Efficient catalytic transformation of plastic wastes to H₂ and electromagnetic nanocarbon absorbents over molecular-level engineered 3D NiCo/MnO

Dan Xu[1a], Chen Shen[2a], Xingmin Liu[2], Wenjie Xie[2], Hui Ding[1], Marc Widenmeyer[2*], Maximilian Mellin[2], Fangmu Qu[2], Aasir Rashid[2], Guoxing Chen[3], Emanuel Ionescu[2,3], Ye Shui Zhang[1,4], Leopoldo Molina-Luna[2], Jan P. Hofmann[2], Dan J. L. Brett[1], Hongbin Zhang[2], Anke Weidenkaff[2,3]*

[1] Electrochemical Innovation Lab, Department of Chemical Engineering, University College London, London, WC1E 7JE, UK

[2] Institute of Materials Science, Technische Universität Darmstadt, Peter-Grünberg-Str. 2, 64287, Darmstadt, Germany

[3] Fraunhofer Research Institution for Materials Recycling and Resource Strategies IWKS, Brentanostraße 2a, 63755 Alzenau, Germany

[4] School of Engineering, University of Aberdeen, Aberdeen, AB24 3UE, UK

[a] These two authors make equal contribution to this work.

[*] Corresponding authors: Xingmin.Liu@mr.tu-darmstadt.de ; marc.widenmeyer@mr.tu-darmstadt.de

Abstract

The advancement in the pyrolysis-catalysis conversion of waste plastics is currently limited by three problematic issues, namely lack of efficient catalysts, ambiguous catalytic mechanism, and identification of a dedicated application of carbon nanocomposites. Herein, advanced bimetallic NiCo/MnO catalysts were developed via a molecular- and macroscale-level engineering strategy. The best conversion performance among all batches was achieved for a Co:Ni molar ratio of 1:1. When the plastic-to-catalyst ratio is 10.7:1, the H_2 and carbon yields of polyethylene conversion reached 29.8 $mmol/g_{plas}$ and 42.2 wt%, respectively. Density functional theory simulations rationalized the activity of NiCo/MnO catalysts in the dehydrogenation of hydrocarbons. The resulting carbon nanocomposites demonstrated excellent electromagnetic absorption performance with an effective absorption bandwidth of the representative carbon nanocomposites/wax composite of 5.12 GHz and a minimal reflection loss lower than −45 dB. This work provides novel insights for developing advanced catalysts for the pyrolysis-catalysis conversion of waste plastics.

Keywords: Waste plastics; $Ni_xCo_{1-x}Mn_2O_4$ spinels; Carbon nanotube composites; H_2 production; Pyrolysis-catalysis

Graphical abstract：
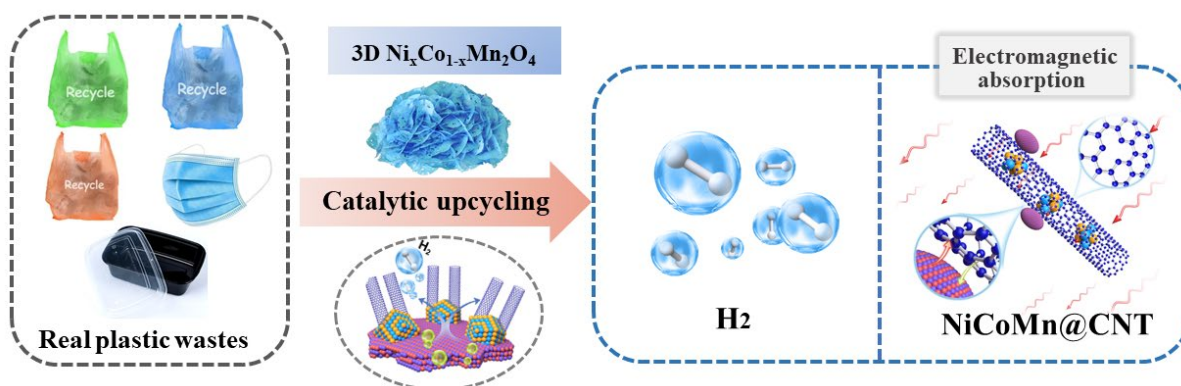
1. Introduction

Global plastic consumption has increased to 359 million metric tons since 2018, leading to a significant growth of plastic wastes (PWs)[1-3]. In 2019, the outbreak of corona epidemic compelled worldwide citizens to produce tremendous medical PWs (e.g., masks, gloves, and syringes)[1-5]. The longevity of PWs in our ecosystems is particularly problematic, which not only pollutes the landscapes and oceans but also leads to a negative impact on flora and fauna[1-3]. To solve this problem, various management ways have been exploited by the research community to realize the potential value of PWs[2, 3]. Among them, the coproduction of hydrogen (H_2) and high-value carbon, namely carbon nanotube composites (CNCs), has been demonstrated to be a promising valorization for the upcycling of waste plastics[2, 3, 6-9].

Recently, with the rapid development of wireless communication technology, the proliferating popularity of electronic equipment has led to inherent electromagnetic irradiation pollution[13-14]. Magnetic nanoparticle modified CNCs (e.g., Ni@CNTs) were proven to be excellent absorbents in electromagnetic shielding applications due to the co-contribution of magnetic loss, conductive loss as well as dielectric loss[15,16]. Furthermore, with great concerns about climate change caused by greenhouse gas emissions from fossil fuels, there is an urgent demand to produce green hydrogen as energy vector to substitute traditional energy sources. Hydrogen can be applied in energy storage and as a valuable feedstock in petroleum refineries, industrial ammonia production, and so on[17,18]. By now, thermochemical conversion of natural gases (e.g., CH_4) is the dominant way for large-scale production of CNTs and H_2, which is energy-intensive and commercially ineffective [2,3]. Hence, the simultaneous production of H_2 and CNCs via pyrolysis-catalysis of plastic wastes provides a sustainable and cost-effective strategy for large-scale industrialization.

60   The features of catalysts (e.g., metal composition, homogeneity, and number of active sites)

61   have been proven to be the most critical factor for recycling efficiency in terms of the yield of

62   CNCs and H_2, as well as the quality of CNCs (e.g., aspect ratio and graphitic degree of CNTs)[2-

63   6,19-23]. Non-noble transition metals (e.g., Fe, Co, and Ni) mixed with support materials (e.g., γ/α-

64   Al_2O_3, SiO_2, and zeolites) are the most widely used pre-catalysts due to the low cost, high catalytic

65   activity and easy processability[2-6,19-23]. However, in pre-catalyst preparation the homogeneous

66   mixing is challenging due to the poor compatibility between the transition metal and support, which

67   decreases the catalytic activity. Moreover, the precise engineering of the nano/microstructure (e.g.,

68   particle size, porosity, and specific surface area) of pre-catalysts via the traditional mixing method

69   has been an unsurmountable challenge, which always results in dense structures and less active

70   sites. To increase the accessible active sites of pre-catalysts, a commonly used way would make

71   the supporting phase account for 90 wt.% of the catalyst [2-6,19-26]. Consequently, the resulting CNCs

72   always possess large amounts of support materials and inferior functional properties, indicating a

73   low commercial value of the CNCs products. Although the purification process of CNCs can be

74   implemented, the processing time and cost will inevitably increase [2,3]. In this circumstance, highly

75   efficient catalysts that can not only achieve high conversion efficiency but also avoid the

76   incorporation of large amounts of inert phase will have to be developed.

77   The multi-scale engineering route (e.g., molecular-level engineering of the composition and

78   nano/micro-level engineering of the structure) was proven to be a promising way for the precise

79   controlling of advanced catalysts[27]. In our former work, multi-scale engineered $Co_xMn_{3-x}O_4$ spinel

80   derived Co/MnO catalysts exhibited outstanding performance with respect to the unprecedently

81   high specific yield of carbon and hydrogen [27]. Notably, due to the excellent integrity of the CNTs

82   and the absence of supporting phases, the produced CNCs exhibited a large aspect ratio and

83 excellent electrochemical performance. Ni has widely been demonstrated as a promising catalyst

84 for hydrocarbon reforming due to the high breakage capability of C-C and C-H bonds[2,3,30,31].

85 Compared to individual metals, bimetallic transition metals catalysts exhibit better performance

86 [6,28,29]. However, the investigation on catalytic conversion of PWs over bimetallic NiCo catalysts

87 has seldom been reported due to the difficulty in engineering on a multi-scale level using classical

88 approaches. Spinel-type oxides possess a general formula of AB_2O_4, where A and B are metal ions

89 (Fe, Co, Ni, Mn, etc.), forming a very large structural family and typically containing one or more

90 metal elements[32-34]. The manifold compositions and various valence states hosted by spinels

91 greatly facilitate the composition engineering (e.g., $Ni_xCo_{1-x}Mn_2O_4$) at the molecular level.

92 Meanwhile, the controllable morphology of spinels will promote the accessibility of active sites to

93 reactants, which makes them a perspective for catalytic pyrolysis of PWs[32-34]. MnO as a catalyst

94 promoter can not only enhance the catalytic performance but also prevent the catalyst from

95 agglomeration[27,35]. Importantly, MnO as a semi-conductive phase can improve the impedance

96 matching of the CNTs-like structure and establish a heterointerface (e.g., MnO-carbon) if it is

97 introduced into the CNCs, which can enhance the electromagnetic absorption capability of the

98 CNCs[36, 37]. Based on those facts, the multi-scale engineered $Ni_xCo_{1-x}Mn_2O_4$ spinels are

99 hypothesized to be promising pre-catalysts in the upcycling of plastic wastes for the simultaneous

100 high-yield production of H_2 and CNCs, and the as-obtained CNCs can be expected to be a powerful

101 electromagnetic absorbent.

102   In this work, multi-scale engineered $Ni_xCo_{1-x}Mn_2O_4$ spinels were developed as bimetallic

103 pre-catalysts via a hydrothermal method. The performance of the $Ni_xCo_{1-x}Mn_2O_4$ derived

104 NiCo/MnO catalysts during thermal conversion of plastic wastes for H_2 and CNCs production was

105 investigated with respect to catalytic reaction temperature, plastic types as well as weight ratio to

106 feedstocks. Density functional theory (DFT) calculations were conducted to reveal the dissociation

107 mechanism of hydrocarbons from decomposed waste plastics, as well as the synergistic interaction

108 of bimetallic NiCo catalysts on the conversion performance. In addition, the growth mechanism of

109 CNTs-like structures on the $Ni_xCo_{1-x}Mn_2O_4$ spinel derived NiCo/MnO catalysts and the application

110 of the produced CNCs as electromagnetic absorbents were investigated in detail.

2. Experimental part

2.1 Chemicals

113 Nickel (II) nitrate hexahydrate ($Ni(NO_3)_2 \cdot 6H_2O$), cobalt (II) nitrate hexahydrate ($Co(NO_3)_2 \cdot 6H_2O$),

114 manganese (II) nitrate hexahydrate ($Mn(NO_3)_2 \cdot 6H_2O$), hexamethylene tetramine (HMTA), and

115 ethanol were supplied by Sigma-Aldrich Chemical Company (Germany). No further purification

116 of the chemical agents was conducted before the experiment. The nomenclature list is summarized

117 in Table S1.

2.2 Synthesis of $Ni_xCo_{-x}Mn_2O_4$ spinels

119 In the present work, flower-like $Ni_xCo_{1-x}Mn_2O_4$ spinels were synthesized via a hydrothermal

120 method. For the $Ni_{0.5}Co_{0.5}Mn_2O_4$ spinel, 1.2 g $Ni(NO_3)_2 \cdot 6H_2O$, 1.2 g $Co(NO_3)_2 \cdot 6H_2O$, and 3.5 g

121 HMTA were dissolved in 50 mL ethanol and 50 mL deionized (DI) water under vigorous stirring.

122 After 10 min, the solution was transferred into a three-neck bottle (250 mL) and heated up to 90

123 °C in a hot air circulation oven. After 12 h, the three-neck bottle was taken out and cooled down to

124 room temperature (25 °C) in the air. The precipitates from hydrothermal synthesis were collected

125 via centrifugation, washed with DI water three times and freeze-dried. The freeze-dried powders

126 were finally calcinated at 550 °C under ambient air atmosphere in a muffle furnace for 3 h. In this

127 work, other batches of spinel-type oxides, namely (i.e., $NiMn_2O_4$, $Ni_{0.33}Co_{0.67}Mn_2O_4$, and

128    $Ni_{0.67}Co_{0.33}Mn_2O_4$) were also prepared. The $NiMn_2O_4$, $Ni_{0.33}Co_{0.67}Mn_2O_4$, and $Ni_{0.67}Co_{0.33}Mn_2O_4$

129   spinels were synthesized by varying the molar ratio of Ni/Co in ethanol-DI water solvent under

130   other identical experimental conditions. Based on the molar ratio of Ni to Co and Mn in the spinels,

131   the $NiMn_2O_4$, $Ni_{0.33}Co_{0.67}Mn_2O_4$, $Ni_{0.5}Co_{0.5}Mn_2O_4$ and $Ni_{0.67}Co_{0.33}Mn_2O_4$ spinels derived catalysts

132   were named as Cat.-Ni_1Mn_2, Cat.-$Ni_{0.33}Co_{0.67}Mn_2$, Cat.-$Ni_{0.5}Co_{0.5}Mn_2$, and Cat.- $Ni_{0.67}Co_{0.33}Mn_2$,

133   respectively.

134   **2.3 Pyrolysis-catalysis conversion**

135   The pyrolysis-catalysis experimental setup is shown in Fig. S1. For the pyrolysis-catalysis

136   reaction, an Al_2O_3 crucible with plastics was placed in the center of the pyrolysis furnace (first

137   stage), and the respective pre-catalysts were placed in the center of the second-stage furnace for

138   the catalytic reaction. The model polyethylene (PE) and post-consumer plastic wastes (including

139   face masks, meal boxes, and plastic bags) were employed as the plastic feedstock to investigate the

140   catalytic properties of as-prepared catalysts in different experimental conditions. The best catalyst

141   with respect to the experimental conditions using PE was identified. After that, the corresponding

142   catalyst was employed under totally identical conditions to convert the post-consumer plastics. The

143   pyrolysis-catalysis conversion reactions were performed with varied parameters, including catalyst

144   composition, the weight ratio of pre-catalysts to waste plastics, and the catalytic reaction

145   temperatures (e.g., 750 $^\circ$C, 800 $^\circ$C, and 850 $^\circ$C), respectively. Before the plastic was heated, the

146   catalysis furnace was preheated to the set temperature (750 $^\circ$C, 800 $^\circ$C, or 850 $^\circ$C) to ensure the

147   readiness of the pre-catalysts. The plastics were heated at a rate of 20 $^\circ$C·min^{-1} from 50 $^\circ$C to 600 $^\circ$C

148   and held at 600 $^\circ$C for 1 h in an Ar atmosphere. During the catalytic transformation, the large

149   condensable molecules from the decomposed plastics were trapped in a condensing system cooled

150   with an ice/water mixture, which can purify the hydrogen-rich gases and protect the equipment

151 from contamination. The non-condensable gases were collected with a Tedlar gas sample bag and

152 analyzed with a gas chromatograph (GC) (Thermo Scientific Trace 1310, Germany). The GC is a

153 dual channel system equipped with Channel A analyzing H_2, CO, and CH_4 using a molecular sieve

154 5 Å column with thermal conductivity detection (TCD) and Channel B analyzing CO_2, C_2H_2, C_2H_4,

155 and C_2H_6 with a polystyrene column and TCD. The carbon yield is calculated by the following

156 equations: carbon yield$=\frac{m_2 - m_1}{m_{feed}} \times 100\%$ (wt.%), specific carbon yield $= \frac{m_2 - m_1}{m_{feed} \times m_{cat}} \times 100\%$ (wt.%).

157 Wherein m_2 and m_1 represent the mass weight of fresh and spent catalysts, respectively; m_{feed} and

158 m_{cat} are the mass weight of plastic waste and catalyst, respectively. The reproducibility of the

159 experimental system is examined, and experiments are repeated to ensure reliability.

160 **2.4 Materials characterization**

161 The size and morphology of the synthesized $Ni_xCo_{1-x}Mn_2O_4$ spinel pre-catalysts and CNCs were

162 characterized via scanning electron microscopy (SEM) (Hitachi, S-4700, Japan). The nanostructure

163 and lattice fingerprint of the $Ni_xCo_{1-x}Mn_2O_4$ spinels, H_2 reduced $Ni_xCo_{1-x}Mn_2O_4$ as well as the

164 CNCs were investigated via transmission electron microscopy (TEM) (JEM2100F, JEOL, Japan).

165 X-ray diffraction (XRD) of the $Ni_xCo_{1-x}Mn_2O_4$ spinels and CNCs was characterized with a STOE

166 X-ray (STOE GmbH & Cie, Darmstadt, Germany) diffractometer in a transmission geometry (Cu

167 $K\alpha_1$ radiation). The crystal structure of the $Ni_xCo_{1-x}Mn_2O_4$ spinels after H_2 exposure at 550 °C was

168 characterized by a STOE STADI MP X-ray diffractometer in a transmission geometry (Mo $K\alpha_1$

169 radiation). Raman spectra of the obtained CNCs were measured with a micro-Raman HR8000

170 spectrometer (Horiba JobinYvon) with a laser wavelength of 514.5 nm from 500 cm^{-1} to 3000 cm^{-}

171 ^{1}. The reduction behavior of the $Ni_xCo_{1-x}Mn_2O_4$ spinels was presented by temperature programmed

172 reduction (TPR) curve via a thermogravimetric analyzer (STA449F3, Netzsch Gerätebau GmbH,

173 Selb, Germany) in a reductive atmosphere (5 vol.% H_2/95 vol.% Ar) with a heating rate of 10

174 $K \cdot min^{-1}$. The carbon content in the CNCs was presented via weight loss behavior as a function of

175 temperature characterized by temperature-programmed oxidation (TPO) by the thermal

176 gravimetrical analysis and differential thermal analysis (TGA–DTA) using a high-temperature

177 simultaneous thermal analyzer (STA449F3, Netzsch Gerätebau GmbH, Selb, Germany) in an

178 oxidation atmosphere (Air) with a heating rate of 10 $K \cdot min^{-1}$. The pore size and specific surface

179 area of the $Ni_xCo_{1-x}Mn_2O_4$ spinels were obtained based on the results of N_2 adsorption/desorption

180 measurements at 77 K by an Autosorb-3B Analyzer (Quantachrome Instruments Corporation).

181 Information on oxidation states, chemical bonding environment, and surface composition of the

182 $Ni_xCo_{1-x}Mn_2O_4$ samples before and after H_2 reduction was obtained with X-ray photoelectron

183 spectroscopy (XPS). All experiments were performed within a vacuum-cluster tool (Thermo Fisher,

184 Escalab 250, USA) with a pressure in the analysis chamber better than $5 \cdot 10^{-10}$ mbar. For excitation,

185 monochromatic Al $K\alpha$ radiation (1486.6 eV) and a spot size of 650 µm were used. All detail spectra

186 were measured by applying a pass energy of 25 eV. A step size of 0.05 eV/step was used. Binding

187 energy calibration was performed with In foil as standard preparation. For O 1s and Ni $2p_{3/2}$ detail

188 spectra, the backgrounds of the acquired spectra were subtracted using the Shirley method in

189 CasaXPS[32], version 2.3.25. Samples were pressed into indium foil. The permittivity, permeability,

190 and S-parameters of the prepared CNCs/wax nanocomposites (mixing ratio 25 wt%:75 wt%) were

191 measured with a coaxial method on a vector network analyzer (VNA, Agilent Technologies

192 E8362B, USA) in the frequency range of 2 GHz to 18 GHz. The obtained CNCs were blended into

193 the wax. The CNCs and wax were shaped by pressing in a plastic mold at room temperature (25 $^\circ$C).

194 **2.5 Computational details**

195 DFT calculations were done using the Vienna Ab-initio Simulation Package code[38, 39]. The

196 exchange correlation interactions and the ion–electron interactions were solved by the Perdew–

197 Burke–Ernzerhof functionals and the projected-augmented wave method[40], respectively. The face

198 centered cubic Ni (111) surface was modeled using 4×4 supercells. For the structure of the solid

199 solution $Ni_{0.5}Co_{0.5}$, special quasi-random structures (SQSs) were employed [41]. These are

200 supercells built in such a way that the correlation functions of a given set of atomic clusters (pairs,

201 triplets, etc.) match those of a true random alloy as closely as possible. A plane-wave cutoff of 600

202 eV was adopted, and the maximal force on all-atoms was below 0.02 eV/Å. The ΔG value can then

203 be determined as follows: $\Delta G = \Delta E + \Delta ZPE - T\Delta S$, where ΔE is the adsorption energy, ΔZPE is the

204 change in zero-point energies, T is the temperature ($T = 298.15$ K), and ΔS is the change of entropy.

205 The adsorption energy ΔE is defined as $\Delta E = E^*_{ads.} - (E^* + E_{ads.})$, where $E^*_{ads.}$ and E^* denote the

206 adsorption of adsorbate on the substrates and bare substrates, respectively, $E_{ads.}$ denotes the energy

207 of the adsorbate. The zero-point energies and entropies of the CH_4 reduction species are determined

208 from the vibrational frequencies in which only the adsorbed species' vibrational modes are

209 computed explicitly with the substrates fixed.

210

211 **3. Results and discussion**

212 **3.1 Characterization of the $Ni_xCo_{1-x}Mn_2O_4$ pre-catalysts**

213 The processing procedure of pyrolysis-catalysis recycling of waste plastics via the $Ni_xCo_{1-x}Mn_2O_4$

214 pre-catalysts as well as the application of obtained CNCs as EM absorbent is schematically

215 presented in Fig. 1a. For the pyrolysis-catalysis conversion, the most critical factor that influences

216 the recycling efficiency of waste plastics is the feature of (pre)catalysts (e.g., composition and the

217   number of active sites). Compared with zero-dimension (0D) nanoparticles and 1D nanowires, 2D

218   nanoflakes of identical materials are expected to exhibit a larger specific surface area and more

219   accessible active sites[32,34]. However, different from other catalytic reactions (e.g., hydrogen

220   evolution reaction and oxygen evolution reaction) where the catalysts were dispersed into an

221   aqueous atmosphere, the catalysts in the pyrolysis-catalysis conversion were typically spread on

222   the fluidized bed. In this circumstance, only one surface can be accessed by the hydrocarbons if

223   2D nanomaterials were employed as catalysts. Compared with 2D structures, 3D structures

224   composed of interlaced 2D nanoflakes will enable more active sites exposed to the hydrocarbons

225   for the pyrolysis-catalysis conversion. Typically, the structure of the targeted pre-catalyst materials

226   is directly determined by the synthesis method[42,43]. Compared with the classical solid phase and

227   vapor deposition synthesis methods, a liquid phase synthesis method, namely hydrothermal

228   synthesis, can facilely control the (nano)structures (e.g., particle size, porosity, morphology, and

229   specific surface area) of the targeted pre-catalysts by operating at relatively low temperature[42,43].

230   In this work, a 3D flower-like porous structure was established in the $Ni_xCo_{1-x}Mn_2O_4$ spinels (Fig.

231   1b-1d, and Fig. S2). The morphology of resultant $NiMn_2O_4$, $Ni_{0.33}Co_{0.67}Mn_2O_4$, $Ni_{0.5}Co_{0.5}Mn_2O_4$,

232   and $Ni_{0.67}Co_{0.33}Mn_2O_4$ spinel pre-catalysts was characterized by SEM (Fig. 1 and S1). As shown

233   in Fig. 1b and Fig. S2(a-c), each $Ni_xCo_{1-x}Mn_2O_4$ spinel particle exhibited a homogeneous 3D

234   flower-like structure in the low magnification SEM images. Interestingly, regardless of the molar

235   ratio of Ni and Co in the spinels, the morphology of the $Ni_xCo_{1-x}Mn_2O_4$ spinels did not exhibit any

236   obvious change. This is a result of the easy substitution of the Ni ions at the *A*-site of the spinel by

237   the Co ions. This property significantly facilitated the molecular-level engineering of the

238   compositions by maintaining the pristine morphology of the spinel particles. In the high

239   magnification SEM images (Fig. 1c and Fig. S2(d-f)), 3D highly porous $Ni_xCo_{1-x}Mn_2O_4$ spinels

240   from self-assembling of 2D nanoflakes were observed, which can effectively prevent the stacking

241   of the 2D nanosheets and expose more active sites to the hydrocarbons during the catalytic

242   conversion. In the high magnification SEM images of nanosheets of $Ni_xCo_{1-x}Mn_2O_4$ spinels, the

243   2D nanosheets exhibited a thickness of 20-30 nm. The porosity of the $Ni_xCo_{1-x}Mn_2O_4$ spinels was

244   characterized by N_2 adsorption/desorption isotherms (Fig. S4). The isotherms of $Ni_xCo_{1-x}Mn_2O_4$

245   exhibited the same tendency with the Type IV characteristic feature, indicating the formation of

246   mesopores in the petals of the flower-like spinels. As shown in Fig. 1d and Fig. S2 (g)-(i), the

247   formation of interlaced 2D nanoflakes generated abundant meso- and macropores which allowed

248   for the interaction of the large-size hydrocarbons (e.g., C10-C20 long-chain alkane and olefins)

249   with the exposed active sites. Figs. S2 (j1)-(j4) show the EDX mapping of the $Ni_{0.5}Co_{0.5}Mn_2O_4$

250   spinel to the corresponding SEM image in Fig. 1c. As expected, strong signals from Ni, Co, Mn,

251   and O were detected in the overlapping area of Fig. S2j. Due to the molecular level engineering,

252   Ni, Co, and Mn were found to homogeneously disperse in the overlap area of Fig. 1c.

253

254
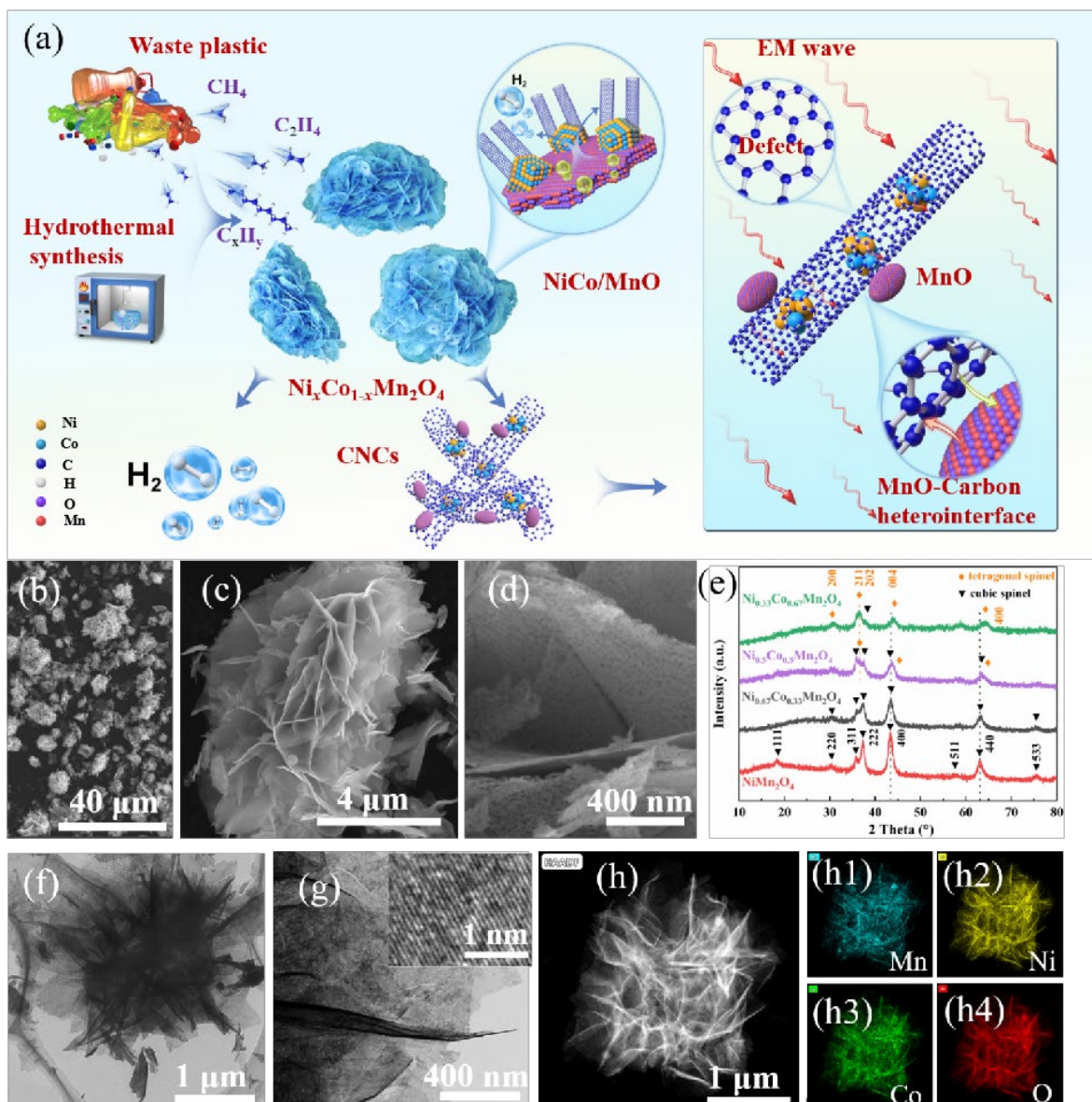
Fig 1. (a) The processing procedure of pyrolysis-catalysis recycling of waste as well as the application of obtained CNCs as EM absorbent, (b) and (c) low magnification SEM image of the $Ni_{0.5}Co_{0.5}Mn_2O_4$ spinel, (d) high magnification SEM image of the $Ni_{0.5}Co_{0.5}Mn_2O_4$ spinel, (e) XRD patterns of as-prepared spinel, (f) low-resolution TEM image of a 3D flower-like $Ni_{0.5}Co_{0.5}Mn_2O_4$ spinel, (g) low-resolution TEM image of a 2D $Ni_{0.5}Co_{0.5}Mn_2O_4$ spinel nanoflake, insert showing

260   the lattice finger print of $Ni_{0.5}Co_{0.5}Mn_2O_4$ spinel, (h) TEM image of the $Ni_{0.5}Co_{0.5}Mn_2O_4$ spinel and

261   (h1-h4) EDX mapping of the $Ni_{0.5}Co_{0.5}Mn_2O_4$ spinel.

262   The composition engineering of catalysts was implemented by the development of spinels with

263   corresponding compositions (Fig. 1e and Fig. S2). In the XRD patterns of $NiMn_2O_4$ spinel (Fig.

264   1e), the characteristic diffraction peaks related to lattice planes (111), (311), (222), (440), and (533)

265   were detected, which confirmed the successful synthesis of cubic $NiMn_2O_4$ spinel[44,45]. However,

266   the 3D flower-like structure as shown in Figure 1 and Figure S1 causes a strong preferred

267   orientation and hence significant variation in the reflection intensity compared to an ideal powder.

268   With the partial substitution of the Ni ions at the *A*-site by Co ions, the corresponding diffraction

269   peaks were shifted gradually to higher angles due to the smaller ionic radius of Co. Notably, at a

270   1:1 ratio of Ni and Co in the spinel ($Ni_{0.5}Co_{0.5}Mn_2O_4$), a characteristic diffraction peak of a

271   tetragonal spinel phase, as also observed for $CoMn_2O_4$, corresponding to the (211) lattice plane

272   appeared next to the cubic spinel phase. With increasing Co content, the tetragonal phase fraction

273   was growing at the expense of the cubic phase. Simultaneously, the degree of preferred orientation

274   was decreased for the samples with Co concentration of ≥50%.

275   The (micro)structure of the representative spinel sample, namely $Ni_{0.5}Co_{0.5}Mn_2O_4$, was observed

276   with the TEM (Fig. 1f-h). In Fig. 1b, a porous flower-like particle with a diameter of 2-3 μm was

277   observed. As can be seen in Fig. 1c-d, the 3D porous structure is composed of 2D nanoflakes with

278   a thickness of 50-100 nm. Fig. S3 depicts multi-scale resolution TEM images of an individual

279    $Ni_{0.5}Co_{0.5}Mn_2O_4$ particle. Fig. S3b and 3c present a few layered nanoflakes of $Ni_{0.5}Co_{0.5}Mn_2O_4$

280   spinel before the formation of the integral flower-like 3D structure, in which stacking of nanoflakes

281   with three to five sheets was observed from lateral and vertical views of the 2D flakes. In Fig. S3c,

282   a stair-like structure was observed due to the different growth speeds of the flakes. Fig. S3d and

283   S3e are the low-resolution TEM images of a monolayer nanoflake. On the surface of the flakes,

284   some small particles or fragments with a size of 100-200 nm were observed. The nanoflakes

285   exhibited different shapes. In Fig. S3d, the nanoflake exhibits a rectangular shape with a length of

286   1.2 μm, while the nanoflakes in Fig. S3e exhibit a fan-like shape. In the higher resolution TEM

287   images (Fig. S3f and 3g), nanoscaled particles with a size of about 30 nm were observed to compose

288   the 2D nanoflakes, which agrees well with the high magnification SEM images. Based on these

289   observations, a growth mechanism of the spinel is proposed, which can be categorized into three

290   steps. In the first step, at the beginning of the hydrothermal synthesis, a complexation reaction

291   between the N-H groups of hexamethylene tetramine and metal ions (e.g., Ni^{2+}, Co^{2+}, and Mn^{2+})

292   occurred and led to the formation of nanosized micelles. Secondly, the hexamethylene tetramine

293   agglomerated the primary particles composed of the metal complexes on the surface of micelles.

294   Due to the shape-inducing effects, these particles were shaped into flat 2D nanosheets[27]. In the

295   third step, when the size in the 2D direction is large enough, new growth of another flake starts

296   from the bottom of the initial flake, which finally leads to the formation of a 3D structure.

297
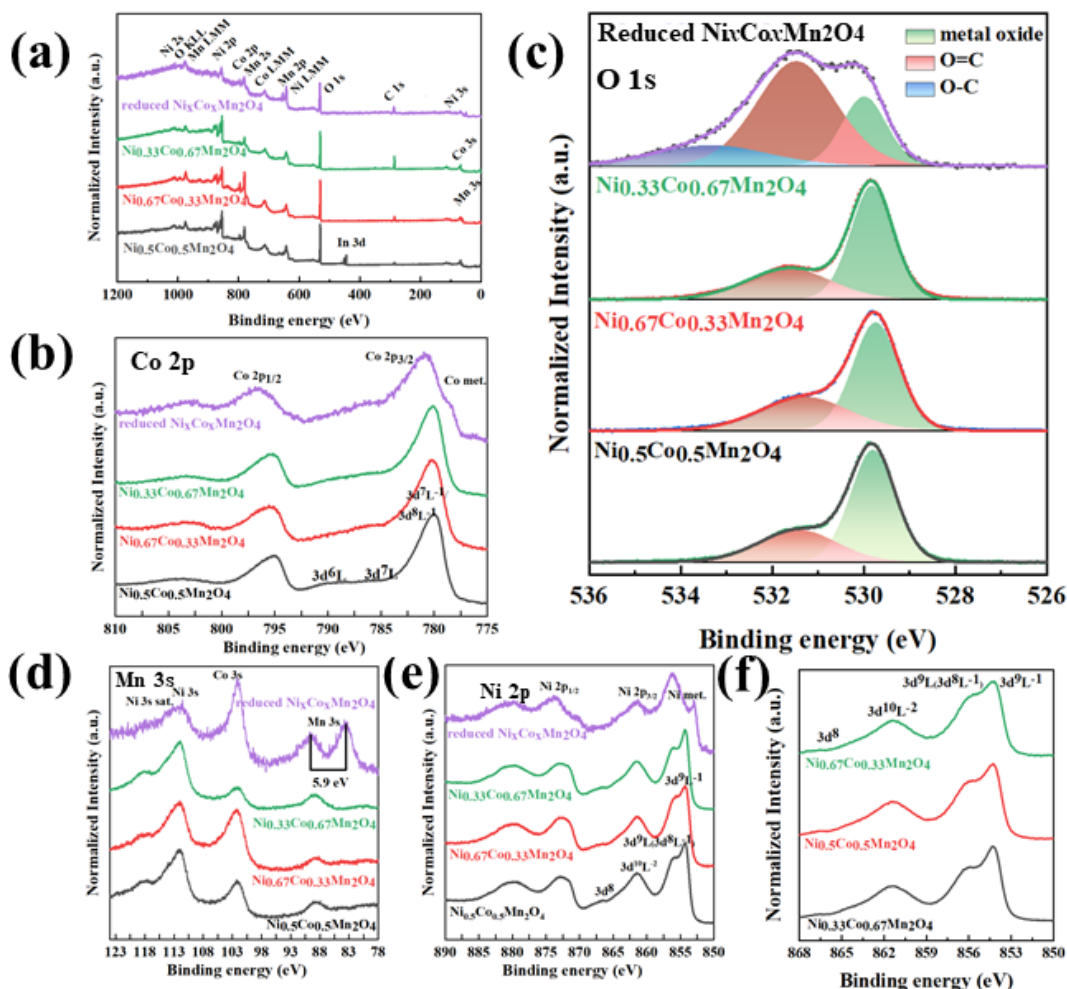
Fig 2. (a) XPS survey spectra, (b) Co 2p spectra, (c) O 1s spectra, (d) Mn 3s, Co 3s, and Ni 3s spectra, (e) Ni 2p of $Ni_xCo_{1-x}Mn_2O_4$, and (f) background-subtracted Ni $2p_{3/2}$ of $Ni_xCo_{1-x}Mn_2O_4$.

The phase composition, chemical environment, oxidation state as well as the pore size and specific surface area of the spinels were characterized by XPS (Fig. 2) and BET (Fig. S4). In the survey XPS spectra of $Ni_xCo_{1-x}Mn_2O_4$ (Fig. 2a), all expected elements were detected, which agrees well with the TEM EDX mapping results (Fig. 1h, Fig. S3 (h1)-(h4), and Fig. 1 (h1)-(h4)). The Co 2p spectra (Fig. 2b) show similar behaviour for all non-reduced samples. Next to the spin-orbit splitting of 15 eV in Co 2p, transition metal oxides show satellites that can be understood by charge-transfer theory[46] multiplet splitting. The main peak at binding energy (BE) (Co $2p_{3/2}$) =

16

308 780 eV can be characterized by the $c^{-1}d^{x+1}L^{-1}$ configuration where c denotes the core hole and

309 $d^{x+1}L^{-1}$ the charge transfer from the ligand to the d-orbital. For the $Ni_xCo_{1-x}Mn_2O_4$ samples, we

310 have identified the main peak as a mixture of d^6L^{-1} and d^7L^{-1} and the satellite at 790 eV as d^6L and

311 at 786 eV as d^7L due to the similar shape and interpretation as for Co_3O_4[27]. Due to the small

312 intensity of the satellites and the overlap with multiple effects, no quantitative analysis of the

313 oxidation state is possible. However, we have concluded that cobalt is in a mixed oxidation state

314 of $2^+/3^+$, equivalent to Co_3O_4. In the reduced sample, all spectra are shifted by about 0.3 eV to

315 higher binding energies due to the charging of the sample. In the Co 2p spectra, a right shoulder

316 appears at 778.5 eV, which indicates the formation of metallic cobalt.

317 The O 1s spectra (Fig. 2c) showed the same components for all materials with the metal oxide peak

318 position at 530.0 eV. The peak at 531.5 eV results from carbonates (O=C) or hydroxides formed at

319 the surface. In the reduced sample, the proportion of carbonates/hydroxides is higher, and

320 additionally an O-C peak is positioned at 533.4 eV, indicating carbon element still remains even

321 after calcination of the spinels. In comparison, the Ni 3s, Co 3s, and Mn 3s (Fig. 2d) can also give

322 information on the oxidation state. For all samples, the Co 3s was found at 102 eV and the Ni 3s at

323 112 eV with a satellite at 118 eV with an intensity ratio of ca. 30 %, which is typical for Ni^{2+}. The

324 Mn 3s can be used to determine the oxidation state of manganese due to the multiplet splitting[47].

325 However, the non-reduced samples only showed one peak at 89.0 eV, but the reason behind this is

326 unclear. In contrast, the reduced sample showed a clear multiple splitting of 5.9 eV, which would

327 indicate an oxidation state close to 2^+. The Ni 2p spectra (Fig. 2e) showed similar behaviour for all

328 non-reduced samples. The main peak was identified as the d^9L^{-1} charge transfer at 854.3 eV, the

329 peak at 856 eV as $d^9L(d^8L^{-1})$ as non-local screening charge transfer, the satellite at 861.5 eV as

330 $d^{10}L^{-2}$, and at 786 eV as d^7L due to the similar shape and interpretation as for NiO[32], which would

17

331   indicate that nickel is in a 2+ state. In the reduced sample, a right shoulder appears at 853.0 eV,

332   which indicates the formation of nickel metal. The Mn 2p spectra (not shown) cannot offer further

333   information about the sample due to the strong overlap with the Ni LMM Auger signal. An

334   interesting feature of the charge-transfer satellites of transition metal oxides (Fig. 2f) showed the

335   change in the intensity ratio of the d^9L^{-1} charge transfer at 854.3 eV to the $d^9L(d^8L^{-1})$ non-local

336   screening charge transfer. The latter describes the charge transfer from the ligand of the next-

337   nearest neighbour. Since the cobalt content is stepwise reduced, more and more nickel is

338   surrounded by cobalt. With cobalt as the next-nearest neighbour the non-local charge transfer is

339   prohibited, and thus the intensity ratio is reduced.

340   **3.2 Products analysis**

341   Carbon and H_2 yields (CY and HY) have been the widely accepted factors for the evaluation of the

342   conversion efficiency of waste plastics[2,3,27]. However, in the industrial application, CY and HY

343   are not sufficient for understanding the overall conversion performance as a higher CY and HY

344   can be easily achieved by employing a larger amount of catalysts (Table S2), which directly

345   increases the upcycling costs and challenges in the purification of the CNTs. Therefore, a more

346   comprehensive way is to define new factors, namely specific carbon and hydrogen yield (SCY and

347   SHY, CY and HY divided by the weight of the pre-catalyst), which take CY and HY as well as

348   pre-catalyst weight into consideration. Such a parameter will be more valuable for determining the

349   overall performance.
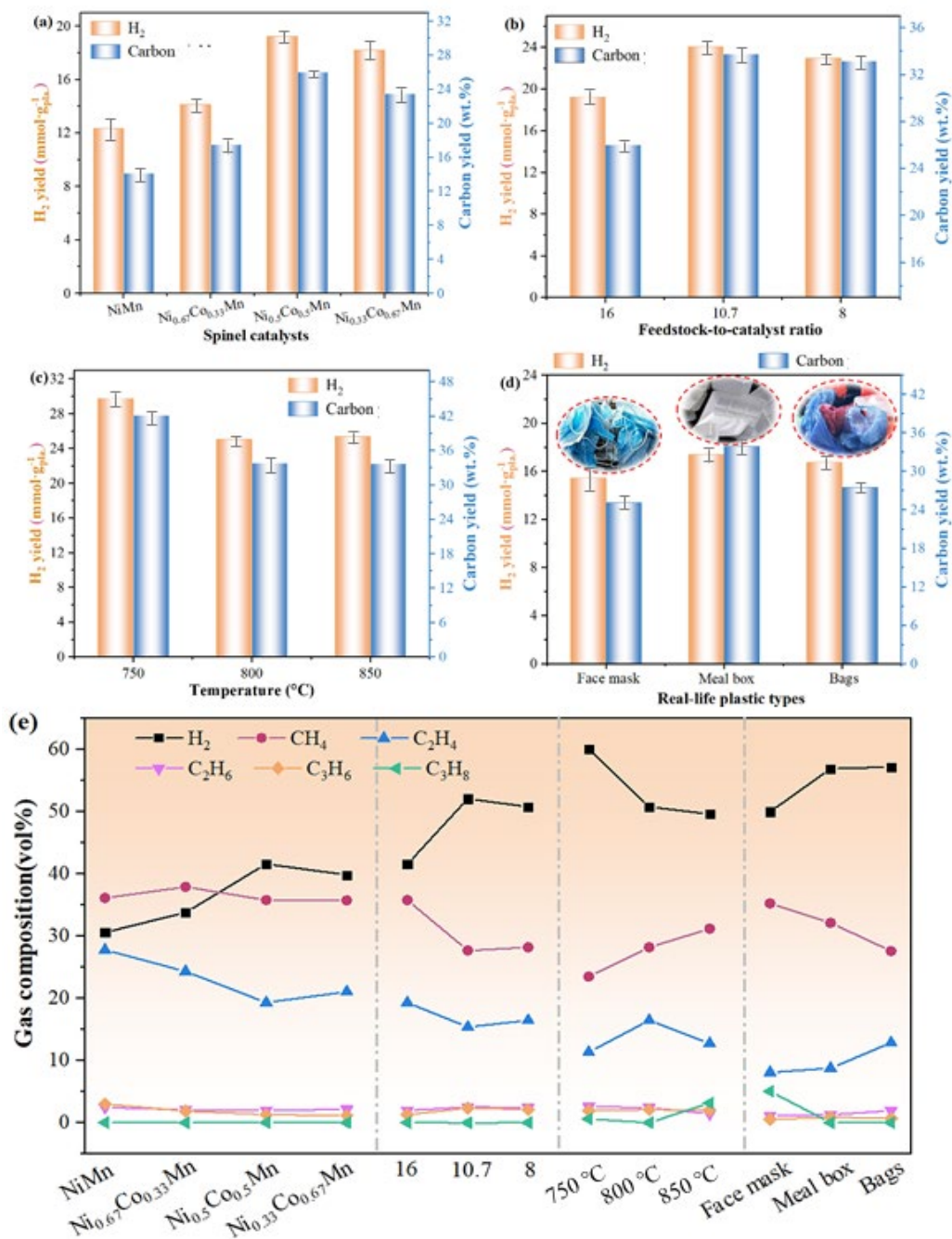
Fig 3. H_2 and carbon yield derived from: (a) Cat.-Ni_1Mn_2, Cat.-$Ni_{0.33}Co_{0.67}Mn_2$, Cat.-$Ni_{0.5}Co_{0.5}Mn_2$, and Cat.-$Ni_{0.67}Co_{0.33}Mn_2$ at a temperature of 800 °C with model PE and a pre-catalyst to the plastic ratio of 1:10.7, (b) Cat.-$Ni_{0.5}Co_{0.5}Mn_2$ with different weight ratios of catalyst to plastic (1:16, 1:10.7, and 1:8) at a temperature of 800 °C, (c) Cat.-$Ni_{0.5}Co_{0.5}Mn_2$ at different temperatures from 750 °C

355   to 850 $^\circ$C with a pre-catalyst to the plastic ratio of 1:8, (d) Cat.-Ni$_{0.5}$Co$_{0.5}$Mn$_2$ with different types

356   of post-consumer plastic at a temperature of 800 $^\circ$C with a pre-catalyst to the plastic ratio of 1:8,

357   (e) gas phase composition of all batches of catalytic reactions with respect to different pre-catalyst

358   types, reaction temperatures, plastic-to-pre-catalyst ratios, and plastic types.

359   Fig. 3(a-e) depict the H$_2$ and carbon yield as well as the gas composition after catalytic conversions

360   with different catalyst compositions, conversion temperatures, weight ratios of feedstock to pre-

361   catalysts, and types of waste plastics. In this work, the most common post-consumer plastic wastes,

362   namely meal boxes, disposable masks, and plastic bags, were also investigated as feedstock for the

363   production of H$_2$ and carbon over the spinel pre-catalysts (Fig. 3d). Fig. 3a presents the H$_2$ and

364   carbon yield achieved by Cat.-Ni$_1$Mn$_2$, Cat.-Ni$_{0.67}$Co$_{0.33}$Mn$_2$, Cat.-Ni$_{0.5}$Co$_{0.5}$Mn$_2$, and Cat.-

365   Ni$_{0.33}$Co$_{0.67}$Mn$_2$ at a temperature of 800 $^\circ$C. At a plastic-to-(pre)catalyst weight ratio of 16:1, the

366   H$_2$ and carbon yield of Cat.-Ni$_1$Mn$_2$ can reach 12.3 mmol/g$_{plas.}$ and 14.1 wt%. With the introduction

367   of Co into catalysts, the H$_2$ and carbon yield increased significantly, which indicates an improved

368   conversion performance. Rising the Co/Ni molar ratio up to 1:1 in the (pre)catalyst

369   (Cat.Ni$_{0.5}$Co$_{0.5}$Mn$_2$), the H$_2$ and carbon yields increased to the maximum values of 19.2 mmol/g$_{plas}$

370   and 26.0 wt%, respectively, under identical conditions (e.g., weight ratio and temperature). With

371   the further increase of the Co/Ni molar ratio to 2:1, the H$_2$ and carbon yield started to decrease,

372   indicating an inferior conversion performance. However, regardless of the Co/Ni molar ratios in

373   the catalysts (Cat.-Ni$_{0.67}$Co$_{0.33}$Mn$_2$, Cat.-Ni$_{0.5}$Co$_{0.5}$Mn$_2$, and Cat.-Ni$_{0.33}$Co$_{0.67}$Mn$_2$), the yields of H$_2$

374   and carbon are always higher than that of the Cat.-Ni$_1$Mn$_2$, indicating a superior catalytic

375   performance of the bimetallic catalysts. The reasons behind this phenomenon are revealed with the

376   assistance of SEM and TEM images of the corresponding CNCs (Fig. S6 and Fig. 4). In the SEM

377   images, after pyrolysis-catalysis, the 3D flower-like structure of the Ni$_x$Co$_{1-x}$Mn$_2$O$_4$ spinels totally

378   disappeared due to the reduction and reactions during the upcycling conversion. During the

379   pyrolysis-catalysis conversion, the oxides of Co and/or Ni in the spinels were firstly reduced into

380   metallic particles before the catalytic reaction, followed by the capturing of hydrocarbons by the

381   Co and/or Ni particles. Even though a high carbon yield was obtained after the catalytic reaction,

382   no filamentous carbon was observed in the carbon composites produced by Cat.-Ni_1Mn_2 (Fig. S6a).

383   In the high magnification SEM image, some worm-like nanomaterials with a length of ~500 μm

384   and a diameter of 100-200 μm were observed. We suggest them to be incompletely developed

385   CNTs (Fig. 4). On the top of the carbon nanomaterials, particles with bright contrast were observed,

386   which is supposed to be agglomerated Ni catalysts. This phenomenon is in accordance with the

387   result of Du et al.[48] With the introduction of Co into the catalyst, filamentous carbon started to be

388   observed in the low magnification SEM image of the carbon nanocomposites using Cat.-

389    $Ni_{0.33}Co_{0.67}Mn_2$. However, the agglomeration of the catalyst is still very serious, which limits the

390   further growth of the CNTs-like structures. When the molar ratio of Co to Ni increased to 1:1 in

391   the catalyst (Cat.-$Ni_{0.5}Co_{0.5}Mn_2$), filamentous carbon nanomaterials were found to grow

392   everywhere in the observation area. In the high-magnification TEM images (Fig. 4h and 4i), the

393   diameter of the filamentous carbons was found to vary from 50 nm to 150 nm. At the highest Co

394   content in the catalyst (Cat.-$Ni_{0.33}Co_{0.67}Mn_2$), the same phenomenon with the carbon

395   nanocomposite derived from Cat.-$Ni_{0.67}Co_{0.33}Mn_2$ was observed.

396   To further investigate the microstructure of the filamentous carbon nanotubes, representative

397   carbon nanocomposites (produced by Cat.-Ni_1Mn_2, Cat.-$Ni_{0.67}Co_{0.33}Mn_2$, and Cat.-$Ni_{0.5}Co_{0.5}Mn_2$)

398   were characterized by TEM. In the low-resolution TEM image of the Cat.-Ni_1Mn_2 derived carbon

399   nanocomposites, agglomerated catalysts as well as short carbon nanomaterials, were observed.

400   Based on the literature[2,3], the agglomeration of catalysts could lead to deactivation, which

401 seriously limits the growth of carbon nanotube-like structures[36-38]. In the high-resolution TEM

402 image, some particles with diameters of 50–200 nm and dark contrast were observed in the carbon

403 nanotube composites (Fig. 4a-4c). This phenomenon can be explained by the serious agglomeration

404 of catalysts, which limited the growth of the CNTs-like structure. Interestingly, the particles with

405 diameters of lower than 100 nm were found to insert in the carbon nanotubes, while those with

406 larger diameters were found to be adjacent to the filamentous materials. Based on our former

407 work[22,27], the particles inserted in the carbon nanotubes should be NiCo catalysts, while the larger

408 particles adjacent to the carbon nanotubes are composites of NiCo/MnO. The existence of the MnO

409 phase could improve the impedance matching of the carbon nanotubes and NiCo metals, as well as

410 form MnO-carbon and MnO-NiCo hetero nanointerfaces, which will lead to interface polarization

411 loss. Moreover, the formation of magnetic NiCo and MnO nanoparticles will contribute to the

412 magnetic loss. The establishment of multiloss mechanisms will undoubtedly lead to the

413 improvement of electromagnetic performance. Due to the introduction of the Co element, the

414 agglomeration of the catalyst was somehow prohibited. Meanwhile, the morphology of each

415 individual CNT exhibited a smoother surface. Fig. 4g, filamentous carbon materials with a length

416 of a few micrometers were observed. In Fig. 4h, we can see that the diameter of these nanomaterials

417 was around 30 nm to 50 nm, which agrees well with the SEM images. Meanwhile, a hollow

418 structure of the nanomaterials can be clearly seen, which confirms them to be CNTs-like. Moreover,

419 the "joint" of the different CNT segments was observed, which can be explained by the "particle-

420 wire-tube" growth mechanism of the CNTs-like structure[49,50]. In the high-resolution TEM image

421 (Fig. 4i), the lattice structure of the graphitic carbon was observed, and the CNTs-like structure

422 was confirmed to be multi-walled.

423
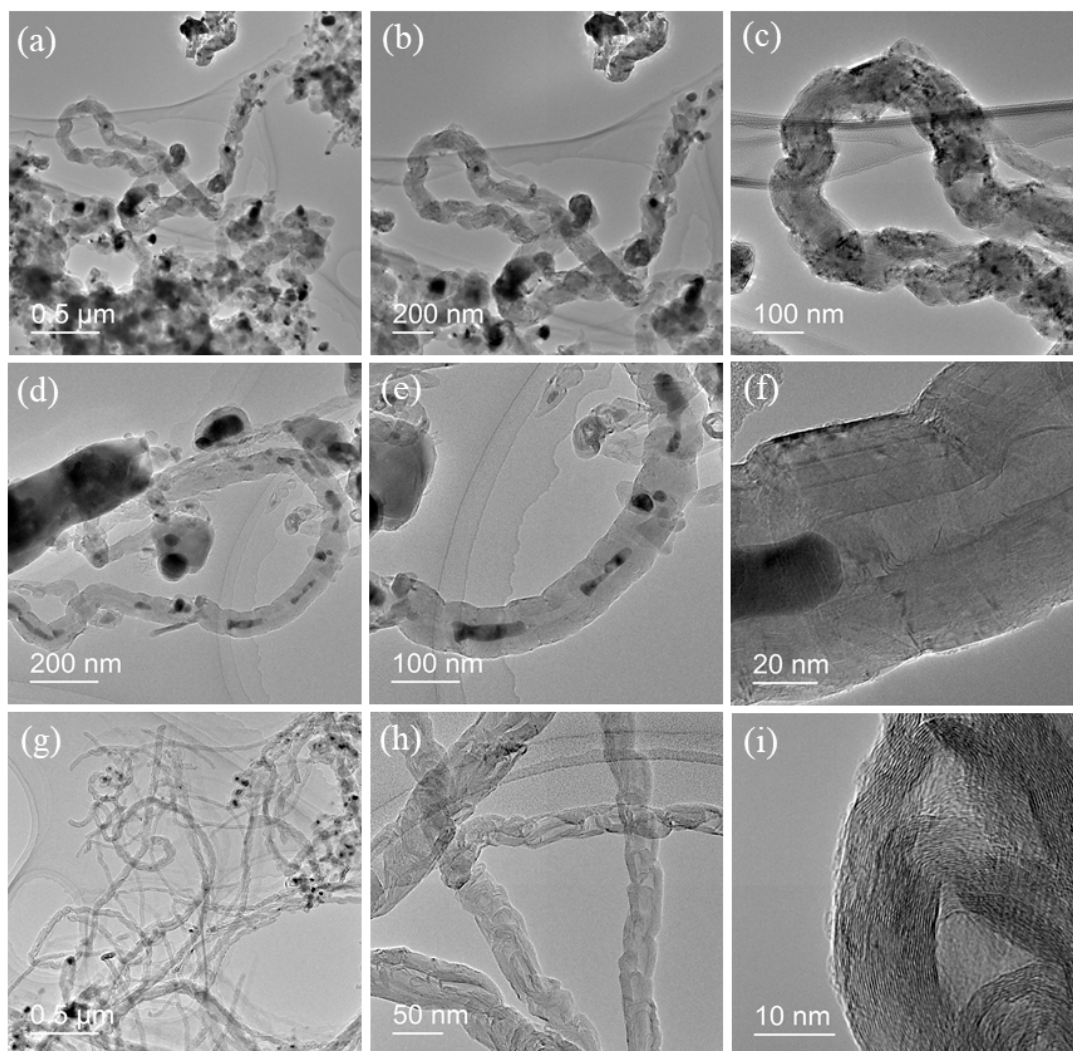
Fig 4. (a) low, (b) and (c) high-resolution TEM images of the CNCs produced by Cat.-Ni_1Mn_2, (d) low, (e) and (f) high-resolution TEM images of the CNCs produced by Cat.-$Ni_{0.33}Co_{0.66}Mn_2$, (g) low, (h) and (i) high-resolution TEM images of the CNCs produced by Cat.-$Ni_{0.5}Co_{0.5}Mn_2$.

To maximize the upcycling efficiency, the H_2 and carbon yields of Cat.-$Ni_{0.5}Co_{0.5}Mn_2$ with respect to plastic/pre-catalyst ratio and reaction temperature were studied (Fig. 3b and 3c). Fig. 3c presents the H_2 and carbon yield of Cat.-$Ni_{0.5}Co_{0.5}Mn_2$ (plastic to pre-catalyst ratio amounts 10.7:1) as a function of temperature. With the increasing conversion temperature, the catalytic performance of Cat.-$Ni_{0.5}Co_{0.5}Mn_2$ decreased gradually, which can be reflected by the corresponding H_2 and carbon

432 yield. At a temperature of 750 $^{\circ}$C, the H_2 and carbon yield reached 29.8 mmol/g_{plas} and 42.2 wt%,

433 respectively, when the plastic to pre-catalyst ratio was 10.7:1. When the temperature increased to

434 850 $^{\circ}$C, the H_2 and carbon yield decreased to 25.8 mmol/g_{plas} and 33.2 wt%, respectively. However,

435 from the SEM images (Fig. 5) of the CNCs, we can see that even though the carbon yield achieved

436 at 750 $^{\circ}$C is higher than at 800 $^{\circ}$C, the CNTs-like structures produced at 800 $^{\circ}$C exhibited better

437 quality in terms of graphitic degree and aspect ratio in Fig. 6 and 7, which is positively correlated

438 with EM absorption performance. XRD results (Fig. 6) demonstrated that NiCo oxides in spinel

439 catalysts were reduced to metallic NiCo alloys during a hydrocarbon reducing environment.

440 Subsequently, NiCo nanoparticles separate gradually from the Co/MnO composites, which leads

441 to the final collapse of the 3D porous structure of the spinels, as observed in Fig. 4 and 5. At a

442 temperature of 850 $^{\circ}$C, serious agglomeration was found in the SEM images of the CNCs. The

443 agglomeration of catalysts resulted from high conversion temperature and is responsible for the

444 decrease of carbon and H_2 yields. Fig. 3b shows the H_2 and carbon yield as a function of varied

445 plastic-to-catalyst ratios. By comparison, the preferred plastic-to-pre-catalyst ratio was found to be

446 around 10.7:1, in which the H_2 and carbon yield can reach as high as 24.0 mmol/g_{plas} and 33.8 wt%,

447 respectively, at a temperature of 800 $^{\circ}$C. Whereas the H_2 concentration reached values as high as

448 52.0 vol% at the expense of CH_4 and C_2H_4 (Fig. 3e). Such a relatively low plastic/pre-catalyst ratio

449 proved the excellent conversion efficiency of our catalysts.
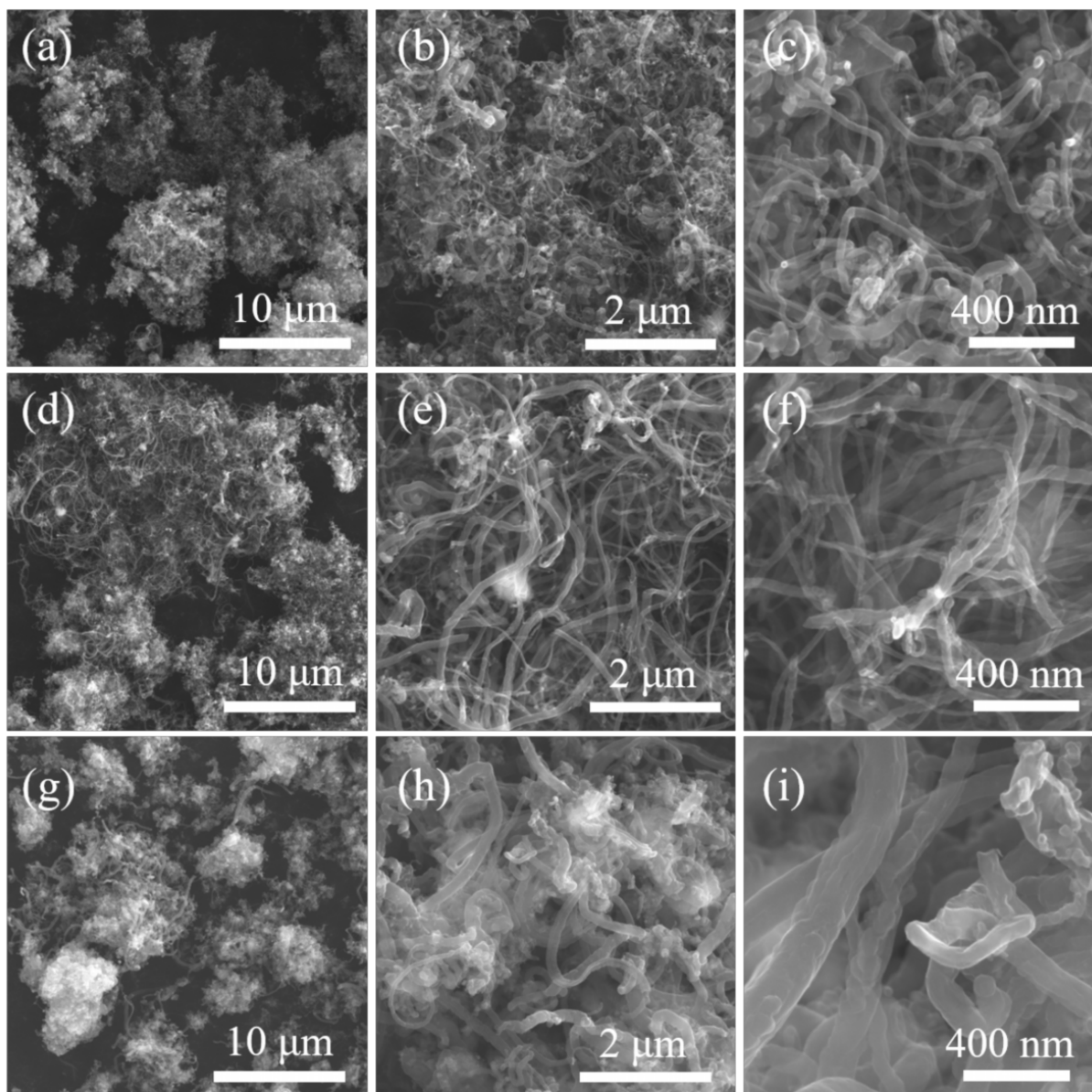
Fig 5. (a) and (b) Low and (c) high magnification SEM images of CNCs from Cat.-$Ni_{0.5}Co_{0.5}Mn_2$ produced at a temperature of 750 $^\circ$C, (d) and (e) low and (f) high magnification SEM images of CNCs from using Cat.-$Ni_{0.5}Co_{0.5}Mn_2$ at a temperature of 800 $^\circ$C, (g) and (h) low and (i) high magnification SEM image of CNCs from Cat.-$Ni_{0.5}Co_{0.5}Mn_2$ produced at a temperature of 850 $^\circ$C. In all cases, PE was used as model plastic waste at a feedstock-to-(pre)catalyst ratio of X:1.

456 In order to find the potential application of the catalysts in the industrialization of post-consumer

457 plastic wastes thermal recycling, three typical municipal plastic wastes, including face masks (FM),

458 meal boxes (MB), and plastic bags (PB) were collected and converted by Cat.-$Ni_{0.5}Co_{0.5}Mn_2$ at

459 800 $^\circ$C and a plastic/pre-catalyst ratio of 8:1. As displayed in Fig. 3d, the H_2 yield of FM, MB, and

460 PB reached 15.4, 17.4, and 16.7 mmol/g, respectively, while the corresponding carbon yield

461 reached 25.1, 33.9, and 27.52 wt%. The H_2 concentration accounted for the primary proportion

462 (>50 vol%) in the gas products (Fig. 3e). Fig. 8 shows the SEM images of the CNCs derived from

463 different types of waste plastics. Interestingly, the morphology (Fig. 8a, 8d, and 8g) as well as the

464 graphitic degree (Fig. 6 and Fig. 7) of the CNCs varies with the variation of the plastic types even

465 under totally identical reaction conditions. Among these three post-consumer plastic feedstocks

466 derived CNCs, the CNCs derived from the plastic bags exhibit the best structure (e.g., aspect ratio

467 and graphitic degree). We suggest this phenomenon may result from the influence of the impurities

468 in the post-consumer waste on the performance of the catalyst.
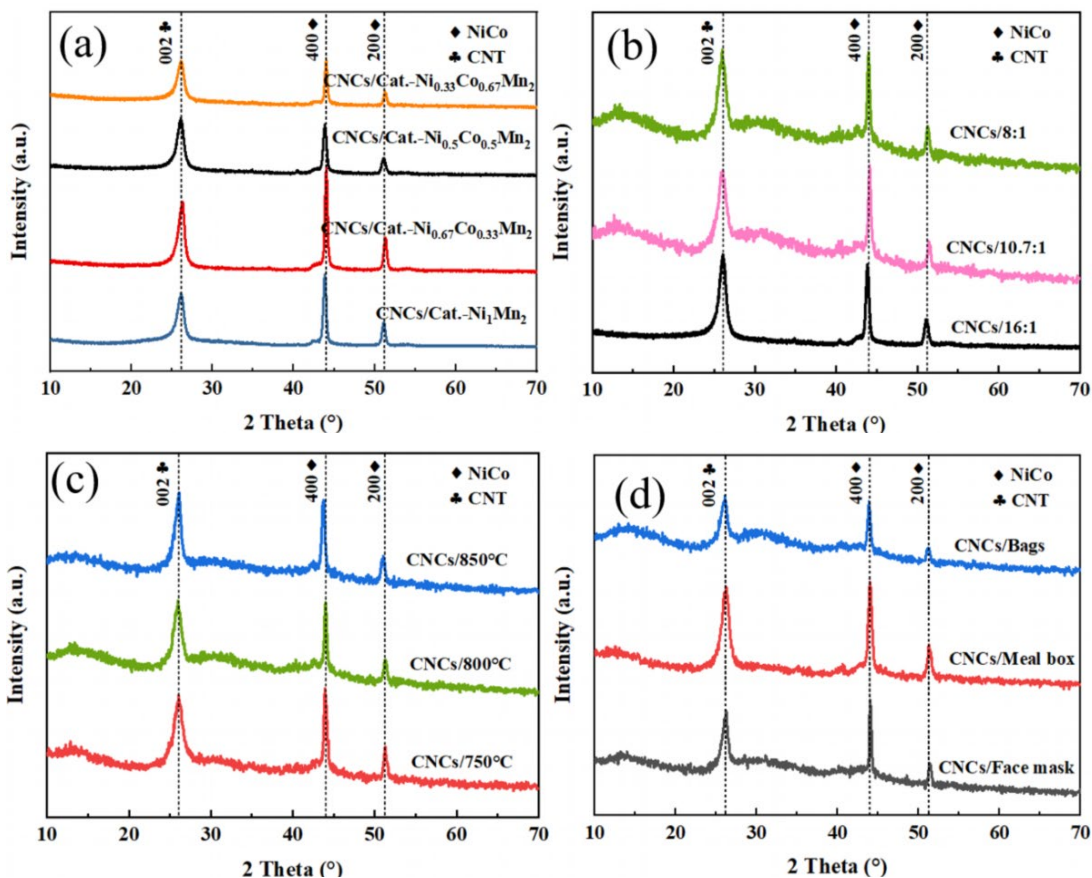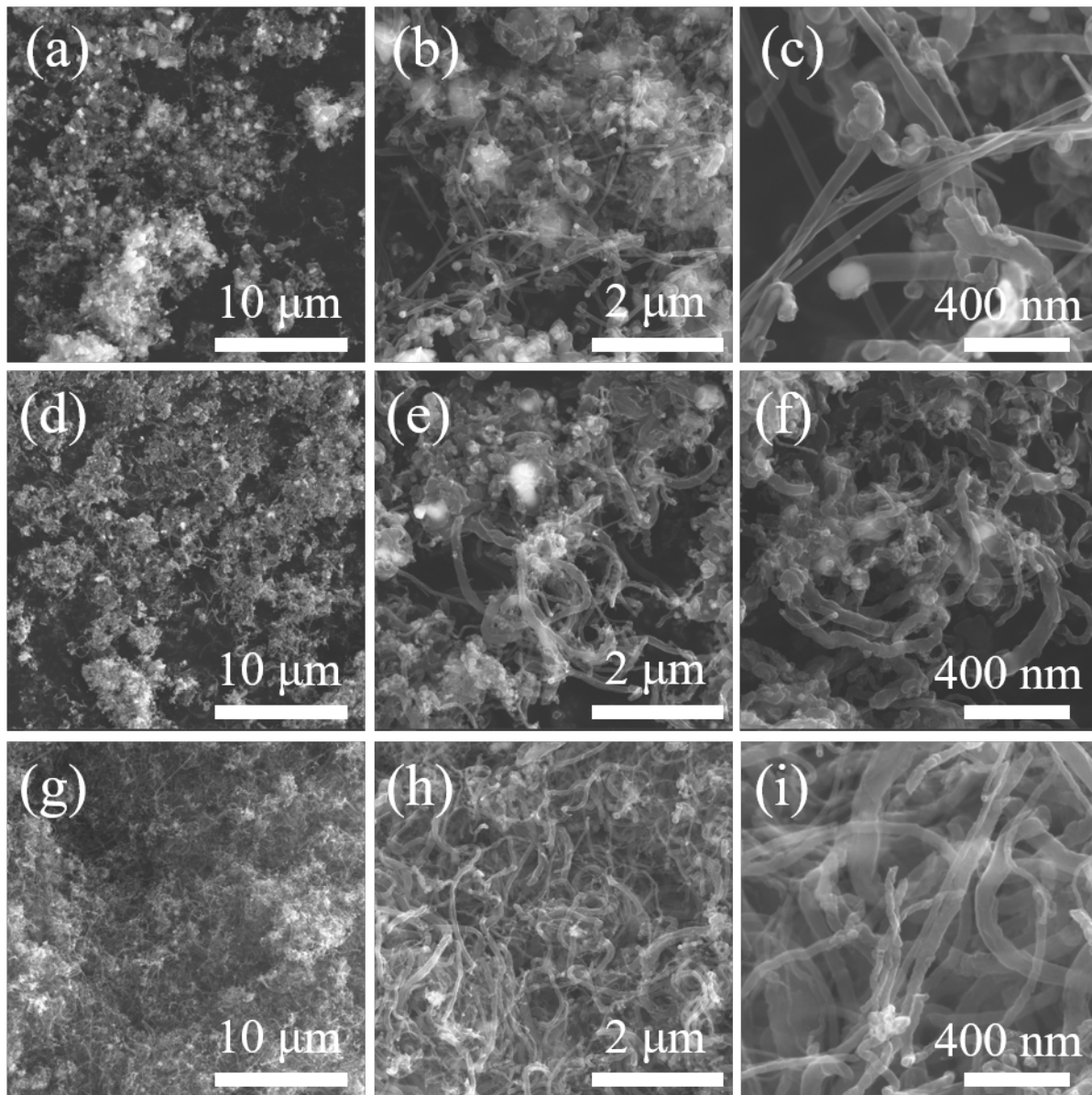
469

470

471 Fig. 6 XRD patterns of the CNCs (a) prepared by Cat.-Ni_1Mn_2, Cat.-$Ni_{0.33}Co_{0.67}Mn_2$, Cat.-

472 $Ni_{0.5}Co_{0.5}Mn_2$, and Cat.-$Ni_{0.67}Co_{0.33}Mn_2$, at 800 °C with model PE and a pre-catalyst to plastic ratio

473 of 1:10.7, (b) by Cat.-$Ni_{0.5}Co_{0.5}Mn_2$ at 800 °C with different pre-catalyst to plastic ratio (1:16,

474 1:10.7, and 1:8), (c) by Cat.-$Ni_{0.5}Co_{0.5}Mn_2$ at 750 °C, 800 °C, and 850 °C with a pre-catalyst to

475 plastic ratio of 1:8, (d) by Cat.-$Ni_{0.5}Co_{0.5}Mn_2$ at 800 °C from post-consumer plastic bags, meal

476 boxes, and face masks with a pre-catalyst to plastic ratio of 1:8.
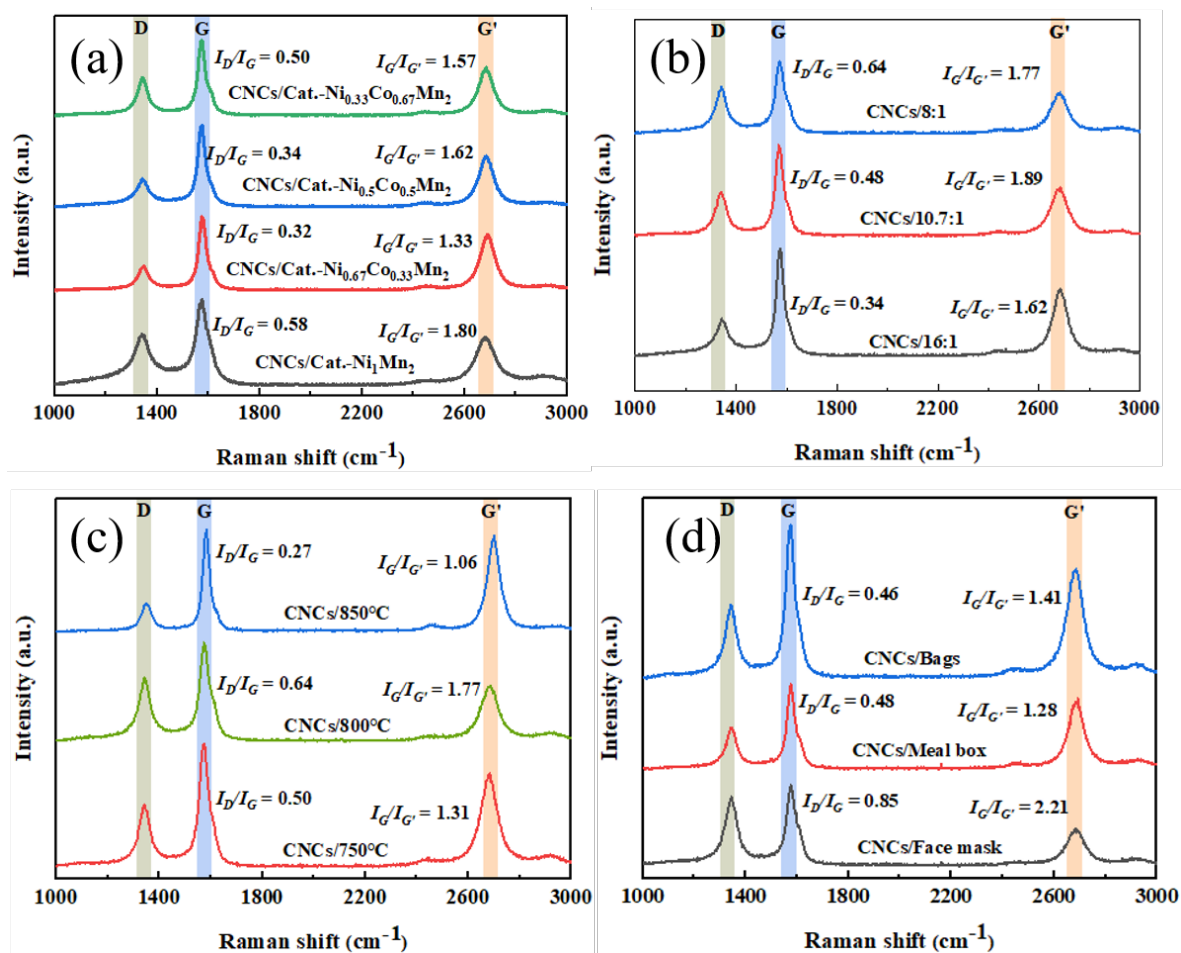
Fig. 7 Raman spectra of the CNCs (a) prepared by Cat.-Ni_1Mn_2, Cat.-$Ni_{0.33}Co_{0.67}Mn_2$, Cat.-$Ni_{0.5}Co_{0.5}Mn_2$, and Cat.-$Ni_{0.67}Co_{0.33}Mn_2$, at 800 °C with model PE and a pre-catalyst to plastic ratio of 1:10.7, (b) by Cat.-$Ni_{0.5}Co_{0.5}Mn_2$ at 800 °C with different pre-catalyst to plastic ratio (1:16, 1:10.7, and 1:8), (c) by Cat.-$Ni_{0.5}Co_{0.5}Mn_2$ at 750 °C, 800 °C, and 850 °C with a pre-catalyst to plastic ratio of 1:8, (d) by Cat.-$Ni_{0.5}Co_{0.5}Mn_2$ at 800 °C from post-consumer plastic bags, meal boxes, and face masks with a pre-catalyst to plastic ratio of 1:8.

Fig 8. (a) and (b) low and (c) high magnification SEM image of CNCs produced by Cat.-$Ni_{0.5}Co_{0.5}Mn_2$ at a temperature of 800 °C with face masks, (d) and (e) low and (f) high magnification SEM image of CNCs from Cat.-$Ni_{0.5}Co_{0.5}Mn_2$ at a temperature of 800 °C with meal boxes, (g) and (h) low and (i) high magnification SEM image of CNCs provided by Cat.-$Ni_{0.5}Co_{0.5}Mn_2$ at the temperature of 800 °C with plastic bags.
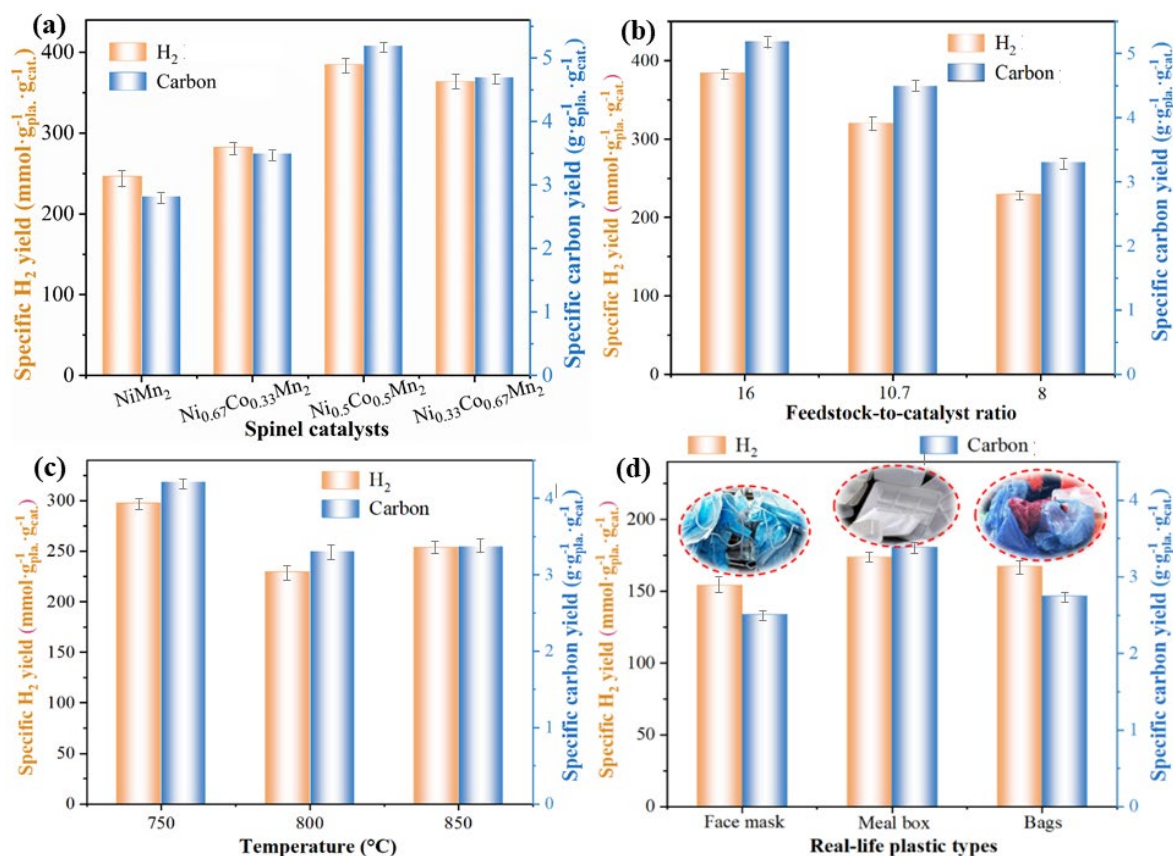
Fig 9. Specific carbon and hydrogen yield of (a) Cat.-Ni_1Mn_2, Cat.-$Ni_{0.33}Co_{0.67}Mn_2$, Cat.-$Ni_{0.5}Co_{0.5}Mn_2$, and Cat.-$Ni_{0.67}Co_{0.33}Mn_2$, (b) with different weight ratios of catalyst to plastic (1:16, 1:10.7, and 1:8) by Cat.-$Ni_{0.5}Co_{0.5}Mn_2$ at a temperature of 800 °C, (c) Cat.- $Ni_{0.5}Co_{0.5}Mn_2$ at different temperatures from 750 °C to 850 °C at a plastic-to-pre-catalyst ratio of 16:1, (d) Cat.-$Ni_{0.5}Co_{0.5}Mn_2$ with different types of post-consumer plastic at a temperature of 800 °C.

Fig. 9 shows the specific carbon and H_2 yields of all conversion reactions achieved under different catalyst compositions, reaction temperatures, plastic/pre-catalyst weight ratios, and plastic types. Due to the high CY and HY of Cat.-$Ni_{0.5}Co_{0.5}Mn_2$, the corresponding SCY and SHY reached 5.2 $g_{cat.}^{-1}$ and 385 $mmol \cdot g_{pla.}^{-1} \cdot g_{cat.}^{-1}$, which is about 5 times higher than reported in the literature (Table S2). With the plastic/pre-catalyst ratio decreasing from 16:1 to 8:1, the value of SCY and SHY has been declining. Despite this, the value of SCY and SHY at a plastic/pre-catalyst

503   ratio of 8:1 still retained 3.4 $g_{cat.}^{-1}$ and 235 $mmol \cdot g_{pla.}^{-1} \cdot g_{cat.}^{-1}$, respectively (Fig. 9b), which is still

504   3 times higher than the reported values. The outstanding SCY and SHY of thermal-catalysis

505   conversion of waste plastics proved the superiority of the catalysts presented in this work. The

506   sustainability of catalysts is very important in the pyrolysis-catalysis upcycling of plastics. In our

507   former work, the cycle performance of catalysts was tested[51]. Unfortunately, limited by the length

508   of this article, the cycle performance of the catalysts with respect to carbon and hydrogen yields

509   will be reported in the following work.

510   **3.3 DFT calculations**

511   To elucidate the dissociation mechanism of hydrocarbons evolved from plastic wastes on spinel-

512   derived catalysts, as well as the synergistic interaction of bimetallic compositions on catalytic

513   performance, DFT calculations on the Cat.-Ni_1Mn_2 and Cat.-$Ni_{0.5}Co_{0.5}Mn_2$ catalyst were conducted

514   in this work. The formation of H_2 and carbon is mainly derived from the C-H and C-C bonds of

515   the hydrocarbons. Hence, the Gibbs free energy profiles were evaluated based on DFT calculations

516   for the five reaction steps of CH_4 dissociation on the Ni (111) and $Ni_{0.5}Co_{0.5}$ (111) surfaces.

517   Considering our experiments were conducted at high temperatures ($T > 600$ °C), CNCs thus

518   predominantly arise from elemental carbon bound to transition metals. Therefore, the transition

519   states of C-H bond cleavage were not considered in this work. For the pristine Ni (111) surfaces,

520   breaking the first C-H bond of CH_4 is needed to overcome a barrier of 0.87 eV, which agrees with

521   the results from Zhu et. al.[52]. The next dehydrogenation step, $*CH_3 \rightarrow *CH_2 + H$, was exothermic

522   with an energy difference of –0.89 eV. The third step for generating *CH consumed only a minor

523   energy of 0.14 eV. The last dehydrogenation step, $*CH \rightarrow *C + H$, was thermodynamically

524   unfavorable and endothermic by 1.33 eV. Hence, this step is the rate-limiting step for CH_4

525   dissociation on Ni (111) surfaces. Compared to the Ni (111) surfaces, 50% Co substitution of Ni

526   gave rise to more versatile surface environments of the $Ni_{0.5}Co_{0.5}$ solid solutions, as shown in Fig.

527   8(b), where the Co and Ni atoms are randomly distributed on the (111) surfaces.

528   To evaluate the activity of the $Ni_{0.5}Co_{0.5}$ (111) surfaces, the surface of the NiCo solid solution was

529   constructed by substituting nearly half of the surface Ni atoms in the Ni (111) unit cell with Co.

530   Considering the disordered arrangement in the NiCo solid solution, we have picked up 11 different

531   active sites for CH_4 dissociation, as shown in Fig. 10(a). The corresponding Gibbs free energy

532   profile of CH_4 decomposition over various active sites is displayed in Fig. 10(b). It was observed

533   that the dissociations on the active site #2 of the solid solutions have similar performance with that

534   of the pristine Ni surfaces, whereas the other active sites in the solid solution all exhibit higher

535   energy differences. Nevertheless, such active sites can be more active for specific steps. For

536   instance, on active site #9, *CH needed lower activation energy (0.12 eV) to finish

537   dehydrogenation. Therefore, this provided a new idea to study the methane dehydrogenation

538   reaction on the solid solution surfaces. Consequently, the reactions do not have to take place at

539   specific Ni or Co atom sites but rather collaboratively at multiple locations, depending on how the

540   corresponding energy difference is. Intermediate products can drift on different active sites to

541   complete the carbon production process with the lowest energy barriers. In addition, various mole

542   ratios of Ni and Co may lead to diverse structural geometries with different defect concentrations.

543   Hence, the solid solutions of $Ni_{0.33}Co_{0.67}$ and $Ni_{0.67}Co_{0.33}$ tend to be relatively ordered phases

544   compared to $Ni_{0.5}Co_{0.5}$. Thus, the more complicated surface environment of $Ni_{0.5}Co_{0.5}$ solid

545   solution provided more comparable active sites for different dehydrogenation steps, which can

546   easily overcome the rate-limiting step[53].
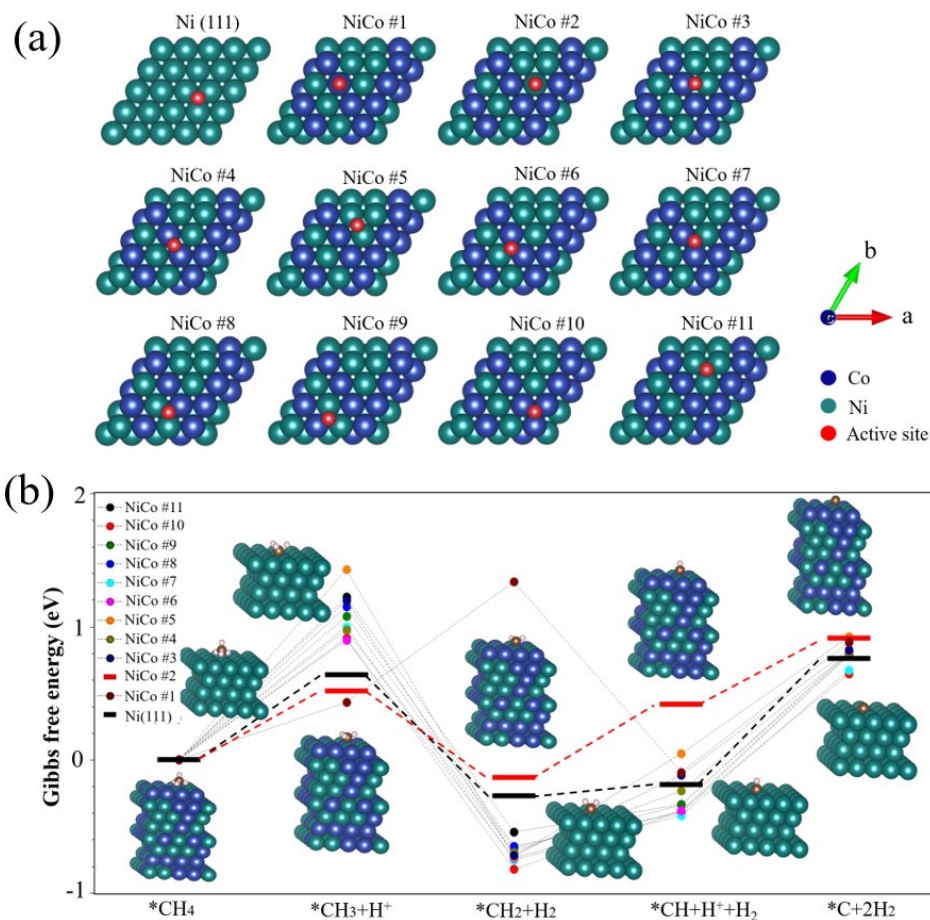
Fig. 10 (a) Corresponding geometries over Ni (111) and $Ni_{0.5}Co_{0.5}$ (111) surfaces, and (b) Gibbs free energy of CH_4 decomposition derived from DFT calculations.

3.4 Electromagnetic properties of the resulting CNCs

To find a dedicated application of the CNCs produced from the waste plastics, electromagnetic properties of the representative CNCs samples were tested by mixing the CNCs in a wax to prepare CNCs/wax composites (weight ratio of CNCs/wax amounts 25 wt%:75 wt%, samples S-1 to S-5). To specify, samples S-1, S-2, and S-3 represent the composites of CNCs produced with Cat.-$Ni_{0.5}Co_{0.5}Mn_2$ at a temperature of 800 $^\circ$C with pre-catalyst to plastic weight ratios of 10.7:1, 16:1,

556 and 8:1, while samples S-4 and S-5 represent the composites of CNCs produced from face masks

557 and meal boxes at a temperature of 800 °C with pre-catalyst to plastic weight ratios of 10.7:1.

558 Fig. 11 presents the real (ε') and the imaginary (ε'') part of the permittivity and tangent loss of the

559 five representative CNCs samples. Theoretically, ε' represents the capability of a material to store

560 electrical energy, while ε'' reflects the capacity to attenuate electromagnetic waves. Dielectric loss

561 (e.g., defects and interfacial induced polarization relaxation), conduction loss, and magnetic loss

562 are the main loss mechanisms for conductive-magnetic electromagnetic absorption materials[54,55].

563 For example, the defects and heterogeneous MnO-carbon interface in the CNCs can lead to

564 polarization loss[54-57]. In this work, the real and the imaginary parts of the permittivity of the

565 samples S-1, S-2, and S-3 exhibited a decreasing tendency due to the decreased carbon content in

566 the corresponding CNCs (Fig. S7). Interestingly, with the same CNCs content in samples S-4 and

567 S-5, the imaginary permittivity of corresponding composites was obviously higher than that of

568 samples S-1, S-2, and S-3. This phenomenon may be attributed to the larger amounts of defects

569 (Fig. 6 and 7) and heterogeneous interface.

570
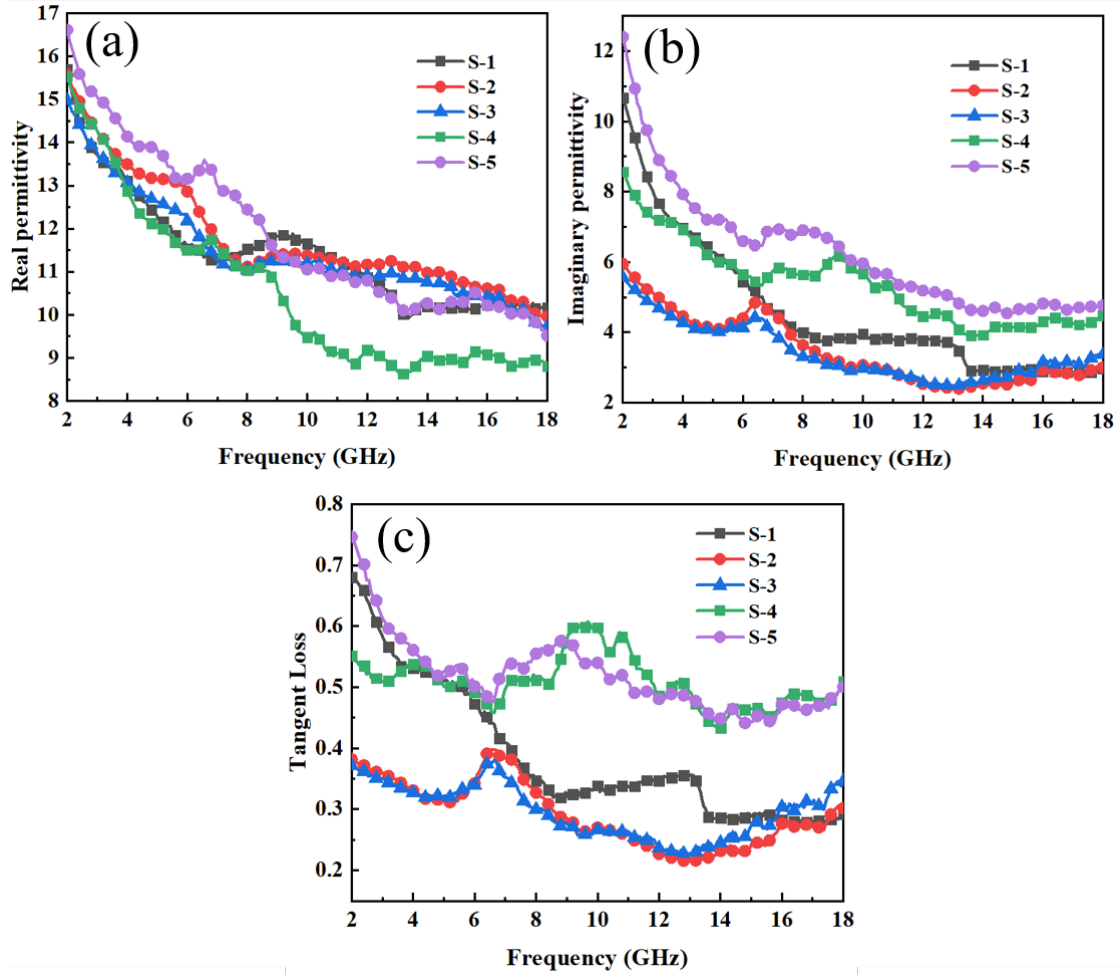
Fig. 11 (a) The real (ε') and (b) the imaginary (ε'') part of the permittivity and (c) tangent loss of the representative CNCs samples.

The electromagnetic absorption capability is characterized by the minimal reflection loss (RL_{min}) and effective absorption bandwidth (EAB)[58-60]. The RL of CNC-based composites was calculated with the following equations 1–3[58-62]:

$$Z = \sqrt{\frac{\mu_r}{\varepsilon_r}} \cdot \tanh\left[j \cdot \frac{2\pi f d}{c} \cdot \sqrt{\mu_r \cdot \varepsilon_r}\right] \qquad 1$$

$$Z_{in} = Z_0 \cdot \sqrt{\frac{\mu_r}{\varepsilon_r}} \cdot \tanh\left[j \cdot \frac{2\pi f d}{c} \cdot \sqrt{\mu_r \cdot \varepsilon_r}\right] \qquad 2$$

$$RL = 20\lg\left|\frac{Z_{in} - Z_0}{Z_{in} + Z_0}\right| \qquad\qquad 3$$

577 where Z_{in}, d, and μ are the normalized input impedance, thickness, and permeability of the material,

578 respectively, c is the light velocity in vacuum, and f is the microwave frequency.

579 Fig. 12 and Fig. S8 present the RL curves of the representative five batches of CNCs composites

580 as a function of the material thickness in the frequency range of 2–18 GHz. As shown in Fig. 12,

581 when the sample thickness is 1.6 mm, the RL_{min} can reach as low as −24.6 dB while the effective

582 absorption bandwidth reached 4.8 GHz from 13.2 GHz to 18 GHz, which is excellent compared

583 with the reported results[64,65]. At a thickness of 2.1 mm, the RL_{min} and EAB values become -18.2

584 dB and 4.1 GHz, respectively. Regardless of the samples, the RL_{min} shifted to a lower frequency

585 area with the increase of material thickness. This phenomenon results from the quarter-wavelength

586 resonant interfering attenuation mechanism of the absorption of EM absorption materials that

587 occurs on the surface[63]. Different from the interaction mechanism of electromagnetic shielding

588 materials, which prevents the EM wave from transmitting, the function of EM absorption materials

589 is to prevent the EM waves from reflection. Due to the similar values of samples S-1, S-2, and S-

590 3, the effective absorption bandwidth of these composites did not exhibit any obvious change. With

591 the increase of the tangent loss in samples S-4 and S-5, the electromagnetic absorption performance

592 improved accordingly. The RL_{min} of sample S-4 can reach as high as −36.8 dB at a thickness of

593 2.15 mm. At a thickness of 1.65 mm, the effective absorption bandwidth reached 5 GHz. As a

594 comparison, the effective absorption bandwidth of sample S-5 reached 5.12 GHz, and the RL_{min}

595 amounts to −24.6 dB at a sample thickness of 1.55 mm, which is even superior to some of the

596 MXene-based materials [64,65].

597
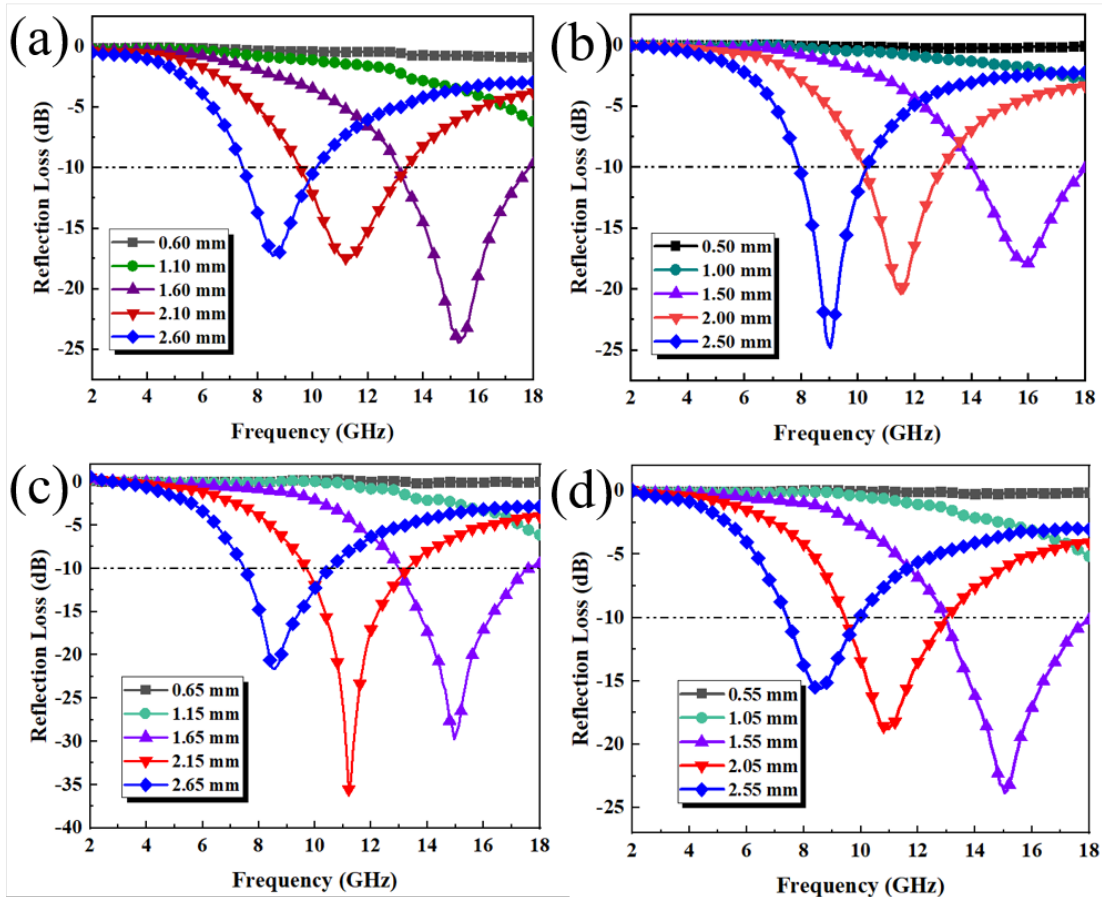
Fig. 12 Reflection loss curves of samples (a) S-1, (b) S-2, (c) S-4, and (d) S-5 from different sample thicknesses.

Besides excellent EM absorption performance, small thickness is also an important factor for the evaluation of electromagnetic absorption materials[64,65]. Fig. 13 shows the 3-D plots and the contour maps of the CNCs/wax nanocomposites as a function of thickness and frequency. As can be seen from the contour maps of the RL plots, the effective absorption bandwidth of the CNCs/wax nanocomposites that is higher than 3 GHz mainly locates between 1.8 mm and 2.5 mm. Compared with other reports[64,65], the thickness of the current CNCs/wax nanocomposites exhibits a superior advantage when they are used as electromagnetic absorption materials.
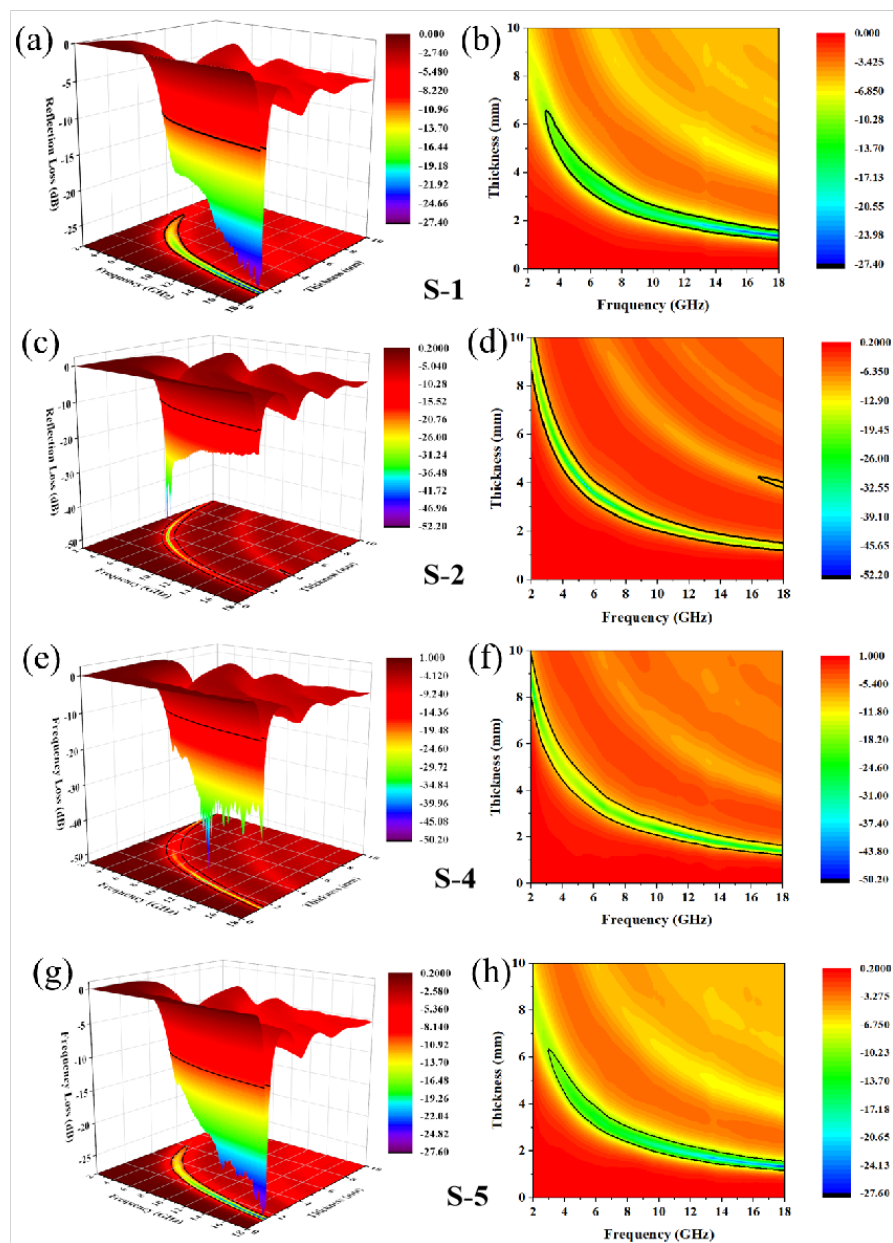
Fig. 13 Three-dimensional (3-D) and two-dimensional plots of the reflection coefficients of samples S-1 (a,b), S-2 (c,d), S-4 (e,f), and S-5 (g,h).

Conclusion

In this work, NiCo-based bimetallic catalysts on MnO were successfully developed via a molecular-level engineering strategy through the preparation of 3D porous $Ni_xCo_{1-x}Mn_2O_4$ spinels.

They were employed as catalysts for the pyrolysis-catalysis conversion of waste plastics for the coproduction of CNCs and H_2. The catalytic performance of the NiCo/MnO catalysts varied with the reaction temperature and composition. At a temperature of 800 $^{\circ}$C, the Cat-$Ni_{0.5}Co_{0.5}Mn_2$ catalyst exhibited the best performance among all prepared catalysts (e.g., Cat.-Ni_1Mn_2, Cat.-$Ni_{0.33}Co_{0.67}Mn_2$, Cat.-$Ni_{0.5}Co_{0.5}Mn_2$, and Cat.-$Ni_{0.67}Co_{0.33}Mn_2$,). When the weight ratio of $Ni_xCo_{1-x}Mn_2O_4$ spinel pre-catalysts to plastic weight ratio is 1:10.7, the HY and CY can reach as high as 29.8 mmol/g_{plas} and 42.2 wt%, while the SHY and SCY reached unprecedented high values of 5.2 $g_{cat.}^{-1}$ and 385 mmol$\cdot g_{pla.}^{-1}\cdot g_{cat.}^{-1}$ for plastic, which is about 5 times higher than the reported in the literature. The DFT calculations revealed that the bimetallic NiCo catalysts provide different active sites than the pure Ni surfaces for the dehydrogenation of hydrocarbons. The resulting CNCs exhibit excellent electromagnetic absorption properties when they are employed as absorbents. This work provided a novel idea for the development of advanced pre-catalysts for the pyrolysis-catalysis of post-consumer plastic waste and finding a new application for the produced CNCs.

Acknowledgments

References

[1] Jiang, J.; Shi, K.; Zhang, X.; Yu, K.; Zhang, H.; He, J.; Liu, J. From plastic waste to wealth

635 using chemical recycling: A review. J. Environ. Chem. Eng. **2022**, *10*, 106867.

636 [2] Zhang, Y.; Zhu, H.; Yao, D.; Williams, P.T.; Wu, C.; Xu, D.; Brett, D. Thermo-chemical

637 conversion of carbonaceous wastes for CNT and hydrogen production: a review. Sustain. Energ.

638 Fuels **2021**, *5*, 4173-4208.

639 [3] Williams, P.T. Hydrogen and carbon nanotubes from pyrolysis-catalysis of waste plastics: A

640 review. Waste Biomass Valor. **2021**, *12*, 1-28.

641 [4] Ding, Z.; Chen, H.; Liu, J.; Evrendilek, F.; Buyukada, M. Pyrolysis dynamics of two medical

642 plastic wastes: Drivers, behaviors, evolved gases, reaction mechanisms, and pathways. J. Hazard.

643 Mater. **2021**, *402*, 123472.

644 [5] Su, G.; Ong, H.C.; Ibrahim, S.; Fattah, I.R.; Mofijur, M.; Chong, C.T. Valorisation of medical

645 waste through pyrolysis for a cleaner environment: Progress and challenges. Environ. Pollut. **2021**,

646 *279*, 116934.

647 [6] Yao, D.; Yang, H.; Hu, Q.; Chen, Y.; Chen, H.; Williams, P.T. Carbon nanotubes from post-

648 consumer waste plastics: Investigations into catalyst metal and support material

649 characteristics. Appl. Catal. B-Environ. **2021**, *280*, 119413.

650 [7] Yao, D.; Wu, C.; Yang, H.; Zhang, Y.; Nahil, M.A.; Chen, Y.; Williams, P.T.; Chen, H.

651 Coproduction of hydrogen and carbon nanotubes from catalytic pyrolysis of waste plastics on Ni-

652 Fe bimetallic catalyst. Energ. Convers. Manage. **2017**, *148*, 692-700.

653 [8] Yao, D.; Wang, C.H. Pyrolysis and in-line catalytic decomposition of polypropylene to carbon

654 nanomaterials and hydrogen over Fe-and Ni-based catalysts. Appl. Energ. **2020**, *265*, 114819.

655 [9] Yao, D.; Zhang, Y.; Williams, P. T.; Yang, H.; Chen, H. Coproduction of hydrogen and carbon

nanotubes from real-world waste plastics: Influence of catalyst composition and operational parameters. Appl. Catal. B-Environ. **2018**, *221*, 584-597.

[10] Herrera-Herrera, A.V.; González-Curbelo, M.Á.; Hernández-Borges, J.; Rodríguez-Delgado, M.Á. Carbon nanotubes applications in separation science: A review. Anal. Chim. Acta **2012**, *734*, 1-30.

[11] Raphey, V.R.; Henna, T.K.; Nivitha, K.P.; Mufeedha, P.; Sabu, C.; Pramod, K.J.M.S. Advanced biomedical applications of carbon nanotube. Mater. Sci. Eng. C **2019**, *100*, 616-630.

[12] Zhang, S.; Nguyen, N.; Leonhardt, B.; Jolowsky, C.; Hao, A.; Park, J.G.; Liang, R. Carbon-Nanotube-Based Electrical Conductors: Fabrication, Optimization, and Applications. Adv. Electron. Mater. **2019**, *5*, 1800811.

[13] Wang, X.X.; Cao, W.Q.; Cao, M.S.; Yuan, J. Assembling nano–microarchitecture for electromagnetic absorbers and smart devices. Adv. Mater. **2020**, *32*, 2002112.

[14] Yan, J.; Zheng, Q.; Wang, S.P.; Tian, Y. Z.; Gong, W.Q.; Gao, F.; Cao M.S. Multifunctional Organic-Inorganic Hybrid Perovskite Microcrystalline Engineering and Electromagnetic Response Switching Multi-Band Devices. Adv. Mater. **2023**, 2300015.

[15] Bai, Y.; Qin, F.; Lu, Y. Lightweight Ni/CNT decorated melamine sponge with sensitive strain sensing performance for ultrahigh electromagnetic absorption in both GHz and THz bands. Chem. Eng. J. **2022**, *429*,132393.

[16] Kumar, R.; Sahoo, S.; Joanni, E.; Singh, R.K.; Tan, W.K.; Kar, K.K.; Matsuda, A. Recent progress on carbon-based composite materials for microwave electromagnetic interference

677   shielding. Carbon **2021**, *177*, 304-331.

678   [17] Abe, J.O.; Popoola, A.P.I.; Ajenifuja, E.; Popoola, O.M. Hydrogen energy, economy and

679   storage: Review and recommendation. Int. J. Hydrogen Energ. **2019**, *44*, 15072-15086.

680   [18] Dawood, F.; Anda, M.; Shafiullah, G.M. Hydrogen production for energy: An overview. Int.

681   J. Hydrogen Energ. **2020**, *45*, 3847-3869.

682   [19] Yao, D.; Li, H.; Mohan, B.C.; Prabhakar, A.K.; Dai, Y.; Wang, C.H. Conversion of Waste

683   Plastic Packings to Carbon Nanomaterials: Investigation into Catalyst Material, Waste Type, and

684   Product Applications. ACS Sustain. Chem. Eng. **2022**, *10*, 1125-1136.

685   [20] Yang, R.X.; Chuang, K.H.; Wey, M.Y. Effects of nickel species on Ni/Al_2O_3 catalysts in

686   carbon nanotube and hydrogen production by waste plastic gasification: bench- and pilot-scale

687   tests. Energ. Fuels **2015**, *29*, 8178-8187.

688   [21] Wu, C.; Williams, P.T. Hydrogen production by steam gasification of polypropylene with

689   various nickel catalysts. Appl. Catal. B-Environ. **2009**, *87*, 152-161.

690   [22] Liu, X.; Xie, W.; Widenmeyer, M.; Ding, H.; Chen, G.; Molina-Luna, L.; De Carolis, D.M ;

691   Riedel, R.; Weidenkaff, A. Upcycling waste plastics into multi-walled carbon nanotube composites

692   via $NiCo_2O_4$ catalytic pyrolysis. Catalysts **2021**, *11*,1353.

693   [23] Wang, J.; Lan, B.; Kang, D.; Wu, C. Carbon nanotubes (CNTs) production from catalytic

694   pyrolysis of waste plastics: The influence of catalyst and reaction pressure. Catal. Today **2020**, *351*,

695   50-57.

696   [24] Gou, X.; Zhao, D.; Wu, C. Catalytic conversion of hard plastics to valuable carbon

697   nanotubes. J. Anal. Appl. Pyrol. **2020**, *145*, 104748.

[25] Cai, N.; Li, X.; Xia, S.; Sun, L.; Hu, J.; Bartocci, P.; Fantozzi, F.; Williams, P.T.; Yang, H.; Chen, H. Pyrolysis-catalysis of different waste plastics over Fe/Al$_2$O$_3$ catalyst: High-value hydrogen, liquid fuels, carbon nanotubes and possible reaction mechanisms. Energ. Convers. Manage. **2021**, *229*, 113794.

[26] Yang, R.X.; Wu, S.L.; Chuang, K.H.; Wey M.Y. Coproduction of carbon nanotubes and hydrogen from waste plastic gasification in a two-stage fluidized catalytic bed. Renew. Energ. **2020**, *159*, 10-22.

[27] Liu, X.; Xu, D.; Ding, H.; Widenmeyer, M.; Xie, W.; Mellin, M.; Hofmann, J.P.; Riedel, R.; Brett, D.J.L.; Weidenkaff, A. Multi-scale designed Co$_x$Mn$_{3-x}$O$_4$ spinels: Smart pre-catalysts towards high-efficiency pyrolysis-catalysis recycling of waste plastics. Appl. Catal. B-Environ. **2023**, *324*, 122271.

[28] Zhou, H.; Saad, J.M.; Li, Q.; Xu, Y. Steam reforming of polystyrene at a low temperature for high H$_2$/CO gas with bimetallic Ni-Fe/ZrO$_2$ catalyst. Waste Manage. **2020**, *104*, 42-50.

[29] Haggar, A.M.; Awadallah, A.E.; Aboul-Enein, A.A.; Sayed, G.H. Non-oxidative conversion of real low density polyethylene waste into hydrogen and carbon nanomaterials over MgO supported bimetallic Co-Mo catalysts with different total Co-Mo contents. Chem. Eng. Sci. **2022**, *247*, 117092.

[30] Dong, H.; Liu, M.; Yan, X.; Qian, Z.; Xie, Y.; Luo, W.; Zhou, Z. Pyrolysis gas from biomass and plastics over X-Mo@MgO (X = Ni, Fe, Co) catalysts into functional carbon nanocomposite: Gas reforming reaction and proper process mechanisms. Sci. Total Environ. **2022**, *831*,154751.

[31] Xu, D.; Xiong, Y.; Ye, J. Performances of syngas production and deposited coke regulation during co-gasification of biomass and plastic wastes over Ni/γ-Al$_2$O$_3$ catalyst: Role of biomass to

720   plastic ratio in feedstock. Chem. Eng. J. **2020**, *392*, 123728.

721   [32] Cheng, Q.; Wang, Z.; Wang, X.; Li, J.; Li, Y.; Zhang, G. A novel $Cu_{1.5}Mn_{1.5}O_4$ photothermal

722   catalyst with boosted surface lattice oxygen activation for efficiently photothermal mineralization

723   of toluene. Nano Res. 2023, *16*, 2133-2141.

724   [33] Cheng, Q.; Li, Y.; Wang, Z.; Wang, X.; Zhang, G. Boosting full-spectrum light driven surface

725   lattice oxygen activation of $ZnMn_2O_4$ by facet engineering for highly efficient photothermal

726   mineralization of toluene. Appl. Catal. B Environ. **2023**, *324*, 122274.

727   [34] Zhao, X.; Mao, L.; Cheng, Q.; Li, J.; Liao, F.; Yang, G.; Chen, L. Two-dimensional spinel

728   structured co-based materials for high performance supercapacitors: a critical review. Chem. Eng.

729   J. **2020**, *387*, 124081.

730   [35] He, S.; Xu, Y.; Zhang, Y.; Bell, S.; Wu, C. Waste plastics recycling for producing high-value

731   carbon nanotubes: Investigation of the influence of Manganese content in Fe-based catalysts. J.

732   Hazard. Mater. **2021**, *402*, 123726.

733   [36] Dong, S.; Tang, W.; Hu, P.; Zhao, X.; Zhang, X.; Han, J.; Hu, P. Achieving Excellent

734   Electromagnetic Wave Absorption Capabilities by Construction of MnO Nanorods on Porous

735   Carbon Composites Derived from Natural Wood via a Simple Route. ACS Sustain. Chem. Eng.

736   **2019**, *7*, 11795-11805.

737   [37] Duan, Y.; Xiao, Z.; Yan, X.; Gao, Z.; Tang, Y.; Hou, L.; Li, Y. Enhanced Electromagnetic

738   Microwave Absorption Property of Peapod-like MnO@carbon Nanowires. ACS Appl. Mater.

739   Interfaces **2018**, *10*, 40078-40087.

740   [38] Kozlov, A.N.E.S.M.; Viñes, F.; Illas, F. Electronic-structure-based chemical descriptors: (in)

741 dependence on self-interaction and Hartree-Fock exchange. Phys. Rev. B **1996**, *54*, 11169-11186.

742 [39] Kresse, G.; Joubert, D. From ultrasoft pseudopotentials to the projector augmented-wave

743 method. Phys. Rev. B **1999**, *59*, 1758.

744 [40] Perdew, J.P.; Ruzsinszky, A.; Csonka, G.I.; Vydrov, O.A.; Scuseria, G.E.; Constantin, L.A.;

745 Burke, K. Restoring the density-gradient expansion for exchange in solids and surfaces. Phys. Rev.

746 Lett. **2008**, *100*, 136406.

747 [41] Zunger, A.; Wei, S.H.; Ferreira, L.G. Bernard, J.E. Special quasirandom structures. Phys. Rev.

748 Lett. **1990**, *65*, 353.

749 [42] Yang, G.; Park, S.J. Conventional and microwave hydrothermal synthesis and application of

750 functional materials: A review. Materials **2019**, *12*,1177.

751 [43] Shi, W.; Song, S.; Zhang, H. Hydrothermal synthetic strategies of inorganic semiconducting

752 nanostructures. Chem. Soc. Rev. **2013**, *42*, 5714-5743.

753 [44] Peng, W.; Chen, K.; Li, S.; Wang, J.; Su, Z.; Song, N.; Xie, A. Spherical spinel $NiMn_2O_4$ in-

754 situ grown on MWCNT via solvothermal synthesis for supercapacitors. Diam. Relat. Mater. **2022**,

755 *128*, 109266.

756 [45] Cabral, A.F.; Remédios, C.M.R.; Gratens, X.; Chitta, V.A. Effects of microstructure on the

757 magnetic properties of polycrystalline $NiMn_2O_4$ spinel oxides. J. Magn. Magn. Mater. **2019**, *69*,

758 108-112.

759 [46] De Groot, F.; Kotani, A. Core level spectroscopy of solids. CRC press (2008).

760 [47] Galakhov, V.R.; Uhlenbrock, S.; Bartkowski, S.; Postnikov, A.V.; Neumann, M.; Finkelstein,

761 L.D.; Leonyuk, L.I. X-ray photoelectron 3s spectra of transition metal oxides. 1999, 9903354.

arXiv preprint cond-mat/9903354.

[48] Du, X.; Yang, L.; Fu, Y.; Liu, S.; Huang, N.; Wang, S. Microwave-Assisted Synthesis of $NiMn_2O_4$ Grown on Nickel Foam as Electrode Material for High-Performance Supercapacitors. Chemistry Select **2021**, *6*, 5567-5574.

[49] Du, G.; Feng, S.; Zhao, J.; Song, C.; Bai, S.; Zhu, Z. Particle-wire-tube mechanism for carbon nanotube evolution. J. Am. Chem. Soc. **2006**, *128*, 15405-15414.

[50] Zhu, Z.; Lu, Y.; Qiao, D.; Bai, S.; Hu, T.; Li, L.; Zheng, J. Self-catalytic behavior of carbon nanotubes. J. Am. Chem. Soc. **2005**, *127*, 15698-15699.

[51] Yu, X; Chen, G.; Widenmeyer, M.; Kinski, I.; Liu, X.; Kunz, U.; Schüpfer, D,; Molina-Luna, L.;Tu, X.; Homm, G.; Weidenkaff, A. Catalytic recycling of medical plastic wastes over $La_{0.6}Ca_{0.4}Co_{1-x}Fe_xO_{3-\delta}$ pre-catalysts for co-production of H2 and high-value added carbon nanomaterials. Appl. Catal. B-Environ., **2023**, *334*, 122838.

[52] Zhu, Y.; Chen, D.; Zhou, X.; Yuan, W. DFT studies of dry reforming of methane on Ni catalyst. Catal. Today **2009**, *148*, 260-267.

[53] Wang, H.; Jiao, Y.; Wu, B.; Wang, D.; Hu, Y.; Liang, F.; Schaaf, P. Exfoliated 2D Layered and Nonlayered Metal Phosphorous Trichalcogenides Nanosheets as Promising Electrocatalysts for CO_2 Reduction. Angewandte Chemie (2023). **https://doi.org/10.1002/ange.202217253**

 [54] Qin, M.; Zhang, L.; Wu, H. Dielectric loss mechanism in electromagnetic wave absorbing materials. Adv. Sci. **2022**, *9*, 2105553.

[55] Gao, Z.; Ma, Z.; Lan, D.; Zhao, Z.; Zhang, L.; Wu, H.; Hou, Y. Synergistic polarization loss of MoS_2-based multiphase solid solution for electromagnetic wave absorption. Adv. Funct. Mater. **2022**, *32*, 2112294.

784 [56] Kong, L.; Yin, X.; Yuan, X.; Zhang, Y.; Liu, X.; Cheng, L.; Zhang, L. Electromagnetic wave

785 absorption properties of graphene modified with carbon nanotube/poly (dimethyl siloxane)

786 composites. Carbon 2014, *73*, 185-193.

787 [57] Kong, L.; Yin, X.; Han, M.; Yuan, X.; Hou, Z.; Ye, F.; Zhang, L.; Cheng L.; Xu, Z. Huang, J.

788 Macroscopic bioinspired graphene sponge modified with in-situ grown carbon nanowires and its

789 electromagnetic properties. Carbon 2017, *111*, 94-102.

790 [58] Gao, Z.; Iqbal, A.; Hassan, T.; Zhang, L.; Wu, H.; Koo, C.M. Texture Regulation of Metal–

791 Organic Frameworks, Microwave Absorption Mechanism-Oriented Structural Optimization and

792 Design Perspectives. Adv. Sci. 2022, 2204151.

793 [59] Zhao, Z.; Zhang, L.; Wu, H. Hydro/organo/ionogels: "controllable" electromagnetic wave

794 absorbers. Adv. Mater. 2022, *34*, 2205376.

795 [60] Liu, Y.; Zhou, X.; Jia, Z.; Wu, H.; Wu, G. Oxygen vacancy-induced dielectric polarization

796 prevails in the electromagnetic wave-absorbing mechanism for Mn-based MOFs-derived

797 composites. Adv. Funct. Mater. 2022, *32*, 2204499.

798 [61] Liu, H.; Zhang, Y.; Liu, X.; Duan, W.; Li, M.; Zhou, Q.; Han, G. Additive manufacturing of

799 nanocellulose/polyborosilazane derived CNFs-SiBCN ceramic metamaterials for ultra-broadband

800 electromagnetic absorption. Chem. Eng. J. 2022, *433*, 133743.

801 [62] Liu, X.; Li, M.; Liu, H.; Duan, W.; Fasel, C.; Chen, Y.; Weidenkaff, A. Nanocellulose-

802 polysilazane single-source-precursor derived defect-rich carbon nanofibers/SiCN nanocomposites

803 with excellent electromagnetic absorption performance. Carbon 2022, *188*, 349-359.

804 [63] Duan, W.; Yin, X.; Li, Q.; Schlier, L.; Greil, P.; Travitzky, N. A review of absorption

805   properties in silicon-based polymer derived ceramics. J. Euro. Ceram. Soc. 2016, *36*, 3681-3689.

806   [64] Cao, M.S.; Cai, Y.Z.; He, P.; Shu, J.C.; Cao, W.Q.; Yuan, J. 2D MXenes: electromagnetic

807   property for microwave absorption and electromagnetic interference shielding. Chem. Eng. J. 2019,

808   *359*, 1265-1302.

809   [65] Song, Q.; Ye, F.; Kong, L.; Shen, Q.; Han, L.; Feng, L.; Li, H. Graphene and MXene

810   nanomaterials: toward high-performance electromagnetic wave absorption in gigahertz band

811   range. Adv. Funct. Mater. 2020, *30*, 2000475.

812

813